Hyperheavy spherical and toroidal nuclei: The role of shell structure

S. E. Agbemava [1,2] and A. V. Afanasjev [1]

[1]*Department of Physics and Astronomy, Mississippi State University, Mississippi 39762, USA*

[2]*Ghana Atomic Energy Commission, National Nuclear Research Institute, P. O. Box LG80, Legon, Ghana*

(Received 7 September 2020; revised 26 December 2020; accepted 16 March 2021; published 25 March 2021)

The properties of toroidal hyperheavy even-even nuclei and the role of toroidal shell structure are extensively studied within covariant density functional theory. The general trends in the evolution of toroidal shapes in the $Z \approx 130$–180 region of the nuclear chart are established for the first time. These nuclei are stable with respect to breathing deformations. The most compact fat toroidal nuclei are located in the $Z \approx 136$, $N \approx 206$ region of the nuclear chart, but thin toroidal nuclei become dominant with increasing proton number and toward proton and neutron drip lines. The roles of toroidal shell structure, its regularity, supershell structure, and shell gaps as well as the role of different groups of the pairs of the orbitals in its formation are investigated in detail. The lowest in energy solutions at axial symmetry are characterized either by large shell gaps or low density of the single-particle states in the vicinity of the Fermi level in at least one of the subsystems (proton or neutron). Related quantum shell effects are expected to act against the instabilities in breathing and sausage deformations for these subsystems. The investigation with a large set of covariant energy density functionals reveals that substantial proton $Z = 154$ and 186 and neutron $N = 228$, 308, and 406 spherical shell gaps exist in all functionals. The nuclei in the vicinity of the combination of these particle numbers form the islands of stability of spherical hyperheavy nuclei. The study suggests that the $N = 210$ toroidal shell gap plays a substantial role in the stabilization of fat toroidal nuclei.

DOI: 10.1103/PhysRevC.103.034323

I. INTRODUCTION

The studies of the nuclei at the limits are guided by human curiosity, by the need to understand new physical mechanisms governing nuclear systems in these extreme conditions, and by the demand for nuclear input in nuclear astrophysics. A number of questions related to the physics at the limits emerge: What are the limits of the existence of nuclei? What are the highest proton numbers Z at which the nuclear landscape and periodic table of chemical elements cease to exist? What are the positions of proton and neutron drip lines? What types of nuclear shapes dominate these extremes of nuclear landscape? They look deceivable simple but unique answers on most of them are extremely difficult.

Recent systematic investigations of hyperheavy ($Z \geqslant 126$) nuclei performed in Refs. [1–3] have allowed to shed some light on these questions. Emerging new physics is summarized in Figs. 1 and 2. The increase of Coulomb interaction with increasing proton number Z leads to the fact that compact nuclear shapes such as spherical, prolate, and oblate (further ellipsoidal-like shapes) become either unstable against fission or energetically unfavored in hyperheavy nuclei with high Z values (see Fig. 1). As a consequence, the lowest in energy solutions in such nuclei are characterized by noncompact toroidal shapes.[1] As illustrated in Fig. 2, the boundary between ellipsoidal-like and toroidal shapes depend on the combination of proton and neutron numbers. However, spherical shapes can be stable against fission in some hyperheavy nuclei (see Refs. [1,2] and Fig. 1). Although these states are highly excited with respect to the lowest in energy states with toroidal shapes (as obtained in axial calculations), they will become the ground states if toroidal states are not stable with respect to multifragmentation.

The state-of-the-art view on the nuclear landscape born out in Refs. [1,2] is shown in Fig. 2. Well-known nuclear structure with pronounced spherical shell gaps at particle numbers 8, 20, 28, 50, 82 (and $N = 126$) leading to the bands (shown by gray color) of spherical nuclei in the nuclear chart along the vertical and horizontal lines with these particle numbers is seen for proton numbers below $Z \approx 120$. With increasing proton number, these classical features disappear and only toroidal shapes are calculated as the lowest in energy in axial relativistic Hartree-Bogoliubov (RHB) approach. This region (shown in white color in Fig. 2) is penetrated only by three islands (shown in gray color) of potentially stable spherical hyperheavy nuclei; note that spherical minima are highly excited with respect to the minima corresponding to toroidal shapes. Thus, the richness of nuclear structure seen in experimentally known part of nuclear landscape is replaced by more uniform structure of the nuclear landscape in the region of hyperheavy nuclei dominated by toroidal and spherical nuclei. Figure 2 also reveals a substantial increase (equal to the area between extrapolated two-proton drip line for ellipsoidal shapes and the two-proton drip line for toroidal shapes) of nuclear landscape caused by the shift of two-proton drip

[1]Toroidal nucleus is represented by a thin cylinder which has the ends joining together [5].

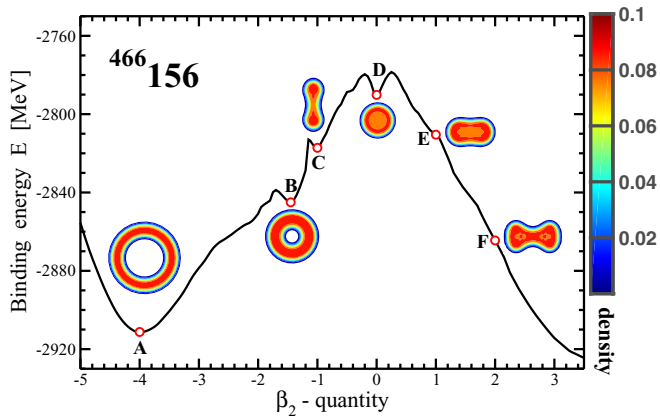

FIG. 1. Schematic illustration of the physics of hyperheavy nuclei. Solid black line shows the deformation energy curve of the $^{466}156$ nucleus obtained in axial relativistic Hartree-Bogoliubov (RHB) calculations with covariant energy density functional (CEDF) DD-PC1 in Ref. [1]. Open red circles indicate selected points on this curve for which neutron density distributions ρ_n are shown. The density distributions in the minima A and B (C, E, and F) are shown in the plane which is perpendicular (along) the axis of symmetry. The density color map starts at $\rho_n = 0.005$ fm^{-3} and shows the densities in fm^{-3}. The density profiles reflect their relative sizes with respect of the spherical shape in the minimum D. See Fig. 9 in the present paper and Fig. 2 in Ref. [2] for these density profiles in their actual sizes.

line toward more proton-rich nuclei on transition to toroidal shapes. This transition drastically modifies the underlying single-particle structure and as a consequence lowers the energy of the Fermi level for protons (see Ref. [3]).

It is necessary to recognize that the physics of toroidal shapes plays an important role in classical and quantum physics, chemistry, and biology. There are numerous examples but let us mention only some of them. Stable toroidal structures (micelles) play an important role in the amphiphilic polymers in large parts of the parameter space spanned by the degree of amphiphilicity, the temperature, the density, and the molecular stiffness with respect to bending [6]. The wave propagation on the surface of the torus represents a vivid example of light behavior on curved surface of manifolds with interesting topologies and has potential applications in photonic structures [7]. The stability of toroidal drop freely suspended in another fluid and subjected to an electric field has been studied in Ref. [8]; this feature can play a role in a number of phenomena and applications such as thunderstorm formation, microfluids, bioimaging, and effective drug delivery. Biology finds the toroidal shape at the cellular level when the reproduction of cells up to the 16th cell division creates a hollow torus called the morula [9]. On a more microsocopic level, the DNA[2] toroids are formed from individual DNA molecules of individual lengths [10].

[2]DNA stands for deoxyribonucleic acid, the molecule that contains the genetic code of organisms.

The question of potential stability of toroidal nuclei was first raised by Wheeler (see references in Ref. [5]). Later, the toroidal shapes in atomic nuclei have been investigated in a number of the papers (see, for example, Refs. [5,11–16] and references quoted therein). However, in an absolute majority of the cases, such shapes correspond to highly excited states either at extreme values of angular momentum in the nuclei across the nuclear landscape [13,14,17] or at spin zero in superheavy elements [12,15]. In the former case, calculated angular momenta at which toroidal shapes appear substantially exceed the values of angular momentum presently achievable at the state-of-art experimental facilities [18]. So far, only the experimental excitation function for the 7α de-excitation of ^{28}Si nuclei, revealing the resonance structures, may indicate the population of toroidal high-spin isomers [19]. In the latter case, such states are unstable in superheavy nuclei against returning to the shape of spherelike geometry (Ref. [15]). This is similar to shrinking instability of uncharged toroidal droplets which are unstable due to surface tension and transform into spherical droplets [20]. The situation is different in atomic nuclei since this shrinking instability is counteracted by Coulomb repulsion of the protons which increases with proton number Z. Thus, toroidal shapes become the lowest in energy solutions in hyperheavy nuclei with $Z > 130$ [1,2,11].

The present paper extends our previous investigations of hyperheavy nuclei reported in Refs. [1,2] and focuses on a number of issues which have not been studied so far. The presence of local minima A, B, C, and D in deformation energy curve of the $^{466}156$ nucleus (see Fig. 1) is clearly due to the shell effects. So far, the underlying single-particle structure has been investigated only for spherical shapes and only for four covariant energy density functionals (see Sec. V in Ref. [2]). To estimate theoretical uncertainties in the predictions of shell closures in hyperheavy nuclei at spherical shape, we perform such studies with the 10 most widely used CEDFs. This also allows us to compare respective spherical shell gaps, leading to the islands of potentially stable spherical hyperheavy nuclei, with the ones seen in experimentally known nuclei as well as with those predicted for spherical superheavy nuclei. In addition, for the first time we perform the detailed investigation of the single-particle structure of hyperheavy toroidal nuclei.

The analysis of the single-particle structure presented in Figs. 5 and 8 of Ref. [2] indicates the presence of large spherical shell gaps at $Z = 186$ and $N = 406$. However, the investigations of Ref. [2] have been restricted to the $Z \leqslant 180$ nuclei. Thus, to better map this region of potentially stable spherical hyperheavy nuclei, to investigate the potential role of these shell gaps, and to search for other regions of potentially stable spherical hyperheavy nuclei, we extended the calculations mapping the nuclear landscape from $Z = 180$ to $Z = 210$.

Finally, because of numerical limitations, the studies of toroidal shapes in hyperheavy nuclei have been with a single exception restricted to the $Z \leqslant 138$ nuclei in Refs. [1,2]. Thus, we performed detailed investigation of toroidal shapes corresponding to the lowest in energy solution at axial symmetry in extremely large basis for isotopic chains with $Z = 136$,

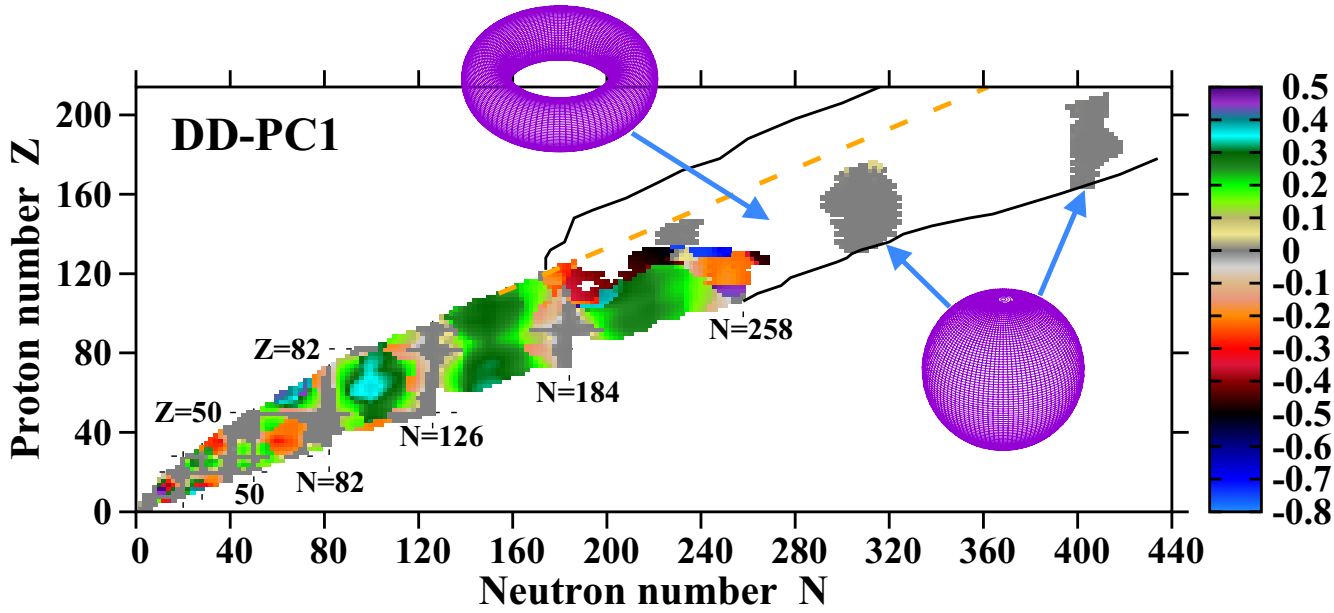

FIG. 2. The distribution of ellipsoidal and toroidal shapes in the nuclear landscape obtained in the RHB calculations with CEDF DD-PC1. The nuclei with ellipsoidal shapes are shown by the squares, the color of which indicates the equilibrium quadrupole deformation β_2 (see color map). Note that ellipsoidal shapes with the heights of fission barriers smaller than 2.0 MeV are considered as unstable (see the discussion in Sec. III of Ref. [4] and Sec. XI of Ref. [2]). Two-proton and two-neutron drip lines for toroidal nuclei are shown by solid black lines. White region between them (as well as the islands inside this region shown in gray) corresponds to the nuclei which have toroidal shapes in the lowest in energy minimum for axial symmetry (LEMAS). The islands of relatively stable spherical hyperheavy nuclei in the $Z > 130$ nuclei, shown in light gray color, correspond to the solutions which are excited in energy with respect of the LEMAS corresponding to toroidal shapes. Note that in the same nucleus two-neutron drip lines for spherical and toroidal shapes are somewhat different. This is the reason why some islands of stability of spherical hyperheavy nuclei extend beyond the two-neutron drip line for toroidal shapes. The extrapolation of the two-proton drip for ellipsoidal shapes, defined from its general trends seen in the $Z < 120$ nuclei, is displayed by thick orange dashed lines. Similar extrapolation for two-neutron drip line of ellipsoidal shapes is close to the two-neutron drip line of toroidal shapes (see Fig. 1 in Ref. [3]); thus, it is not shown. Partially based on Fig. 24 of Ref. [2].

146, 156, 166, and 176. This allows us to better understand their evolution with particle numbers and to get some understanding about their potential stability with respect of different types of distortions.

The paper is organized as follows. The details of theoretical calculations are discussed in Sec. II. Section III is devoted to the analysis of the role of shell structure and large shell gaps at spherical shape. The distribution of the shapes of toroidal hyperheavy nuclei across the nuclear landscape and major features of their shell structure are discussed in Sec. IV. Finally, Sec. V summarizes the results of our work.

II. THE DETAILS OF THE THEORETICAL CALCULATIONS

The investigations of the properties of hyperheavy even-even nuclei are performed within the axial reflection symmetric Hartree-Bogoliubov (RHB) framework (see Ref. [21]). Unless specified otherwise, the calculations are performed with the DD-PC1 covariant energy density functional [22]. This functional is considered to be one of the best CEDFs today based on systematic and global studies of different physical observables related to the ground-state properties and fission barriers [21,23–28].

The constrained calculations in the RHB code perform the variation of the function

$$E_{\rm RHB} + \frac{C_{20}}{2}(\langle\hat{Q}_{20}\rangle - q_{20})^2, \tag{1}$$

where $E_{\rm RHB}$ is the total energy and $\langle\hat{Q}_{20}\rangle$ denotes the expectation value of the mass quadrupole operator,

$$\hat{Q}_{20} = 2z^2 - x^2 - y^2. \tag{2}$$

Here q_{20} is the constrained value of the multipole moment, and C_{20} is the corresponding stiffness constant [29]. In order to provide the convergence to the exact value of the desired multipole moment, we use the method suggested in Ref. [30]. Here the quantity q_{20} is replaced by the parameter $q_{20}^{\rm eff}$, which is automatically modified during the iteration in such a way that we obtain $\langle\hat{Q}_{20}\rangle = q_{20}$ for the converged solution. This method works well in our constrained calculations.

The β_2 quantity is extracted from the quadrupole moments:

$$Q_{20} = \int d^3r\rho(\boldsymbol{r})\,(2z^2 - x^2 - y^2), \tag{3}$$

via

$$\beta_2 = \sqrt{\frac{5}{16\pi}}\frac{4\pi}{3AR_0^2}Q_{20}, \tag{4}$$

where $R_0 = 1.2A^{1/3}$. The β_2 values have a standard meaning of the deformations of ellipsoid-like density distributions only for $|\beta_2| \lesssim 1.0$ values. At higher β_2 values, they should be treated as dimensionless and particle normalized measures of the Q_{20} moments. This is because of the presence of toroidal shapes at large negative β_2 values and necking degree of freedom at large positive β_2 values.

For each nucleus under study, the deformation energy curves are calculated in the $-5.0 < \beta_2 < 3.0$ range; such large range is needed for a reliable definition of the type of shape (toroidal or ellipsoidal) representing the lowest in energy minimum for axial symmetry (LEMAS). Two truncation schemes are used in the calculations based on the analysis presented in Sec. III of Ref. [2] and additional analysis performed in this paper. All states belonging to major shells up to $N_F = 30$ fermionic shells for the Dirac spinors are taken into account when detailed analysis of toroidal shapes in the $Z = 136$–176 region and their underlying shell structure is performed. Note that these calculations are extremely time-consuming. As discussed in detail in Sec. III of Ref. [2] on the example of the $^{466}156$ nucleus and verified by a similar analysis of a pair of the $Z = 176$ nuclei, this basis provides sufficient numerical accuracy of the calculations of toroidal shapes. However, the analysis of numerical convergence in the $^{616}210$ nucleus reveals that the description of higher Z nuclei requires even large N_F for a proper description of LEMAS corresponding to toroidal shapes. These facts were the reasons why we perform detailed study of toroidal shape only up to $Z = 176$ and for $Z > 176$ nuclei we focus mainly on ellipsoidal-like shapes, which require smaller basis as compared with toroidal shapes (see Sec. III of Ref. [2] for a detailed comparison of numerical convergence for toroidal and ellipsoidal-like shapes). To save computational time, the extension (as compared with the results presented in Ref. [2]) of nuclear landscape to the $Z = 182$–210 region is performed with $N_F = 26$; this truncation scheme allows an accurate description of spherical and ellipsoidal shapes, and a reliable definition of toroidal shapes as corresponding to LEMAS, but does not provide an accurate enough description of their energies and shapes in LEMAS.

To avoid the uncertainties connected with the definition of the size of the pairing window [40], we use the separable form of the finite-range Gogny pairing interaction introduced in Ref. [41]. Its matrix elements in $\boldsymbol{r}$ space have the form

$$V(\boldsymbol{r}_1, \boldsymbol{r}_2, \boldsymbol{r}'_1, \boldsymbol{r}'_2) = -G\delta(\boldsymbol{R} - \boldsymbol{R'})P(r)P(r')\tfrac{1}{2}(1 - P^{\sigma}), \quad (5)$$

with $\boldsymbol{R} = (\boldsymbol{r}_1 + \boldsymbol{r}_2)/2$ and $\boldsymbol{r} = \boldsymbol{r}_1 - \boldsymbol{r}_2$ being the center of mass and relative coordinates. The form factor $P(r)$ is of Gaussian shape,

$$P(r) = \frac{1}{(4\pi a^2)^{3/2}} e^{-r^2/4a^2}. \quad (6)$$

The parameters of this interaction have been derived by a mapping of the $^1S_0$ pairing gap of infinite nuclear matter to that of the Gogny force D1S. The resulting parameters are: $G = 728$ fm^3 and $a = 0.644$ fm [41]. This pairing provides a reasonable description of pairing properties in heaviest nuclei in which pairing properties can be extracted from experimental data [21,42,43].

III. SPHERICAL HYPERHEAVY NUCLEI: THE ROLE OF SHELL STRUCTURE

Hyperheavy nuclei are stabilized by shell effects, i.e., by the large shell gap(s) or at least a considerably reduced density of the single-particle states in the vicinity of the Fermi level. To better understand the impact of shell gaps on the underlying structure of spherical nuclei in the context of global description of nuclear structure, Fig. 3 shows their evolution across nuclear chart. It starts from well known gaps in doubly magic ^{56}Ni, ^{100,132}Sn and ^{208}Pb nuclei and extends to the gaps in the hyperheavy nuclei. In addition, it provides the evaluation of theoretical uncertainties in their predictions by comparing the results obtained with ten most widely used CEDFs.

Figures 3(a) and 3(b) show that the average sizes of proton $Z = 154, 186$ and neutron $N = 228, 308$, and 406 gaps obtained in the calculations are larger than those ($Z = 120$ and $N = 184$) in classical region of superheavy nuclei.[3] This suggests that spherical hyperheavy nuclei may be more stable as compared with spherical superheavy nuclei (see the discussion of fission barriers in Refs. [1,2]). It is also interesting that theoretical uncertainties in the sizes of shell gaps in hyperheavy nuclei are smaller than those in experimentally known nuclei and in classical region of superheavy nuclei.

The absolute values of shell gaps do not tell full story about their potential stabilizing effect since the single-particle level density increases with mass number A. This is a reason why scaled shell gap $\Delta E_{\rm gap} A^{1/3}$ provides a better measure (see discussion in Sect. III of Ref. [23]). Scaled proton and neutron shell gaps are shown in Figs. 3(c) and 3(d). One can see that scaled proton $Z = 154$ and 186 shell gaps are significantly larger than scaled $Z = 120$ shell gap in superheavy nuclei and that they are close to the scaled $Z = 82$ shell gap in ^{208}Pb [see Fig. 3(c)]. In contrast, scaled $N = 228, 308$, and 406 shell gaps are on average only slightly larger than scaled $N = 184$ gap in superheavy nuclei but they are smaller by a factor of approximately two than scaled $N = 126$ shell gap in ^{208}Pb [see Fig. 3(d)].

Large uncertainties in the predictions of the $Z = 120$ and $N = 184$ shell gaps and softness of potential energy surfaces leads to substantial differences in the predictions of ground-state properties of superheavy nuclei (see Ref. [23]). For many nuclei, it is even impossible to reliably predict whether the ground state will be spherical or oblate [23]. The situation is different in hyperheavy nuclei where for ellipsoidal type shapes only potentially stable spherical minima appear in the calculations because of larger scaled spherical shell gaps seen in Figs. 3(c) and 3(d).

Figure 4 presents the extension of the map of the heights of fission barriers around spherical shapes from the earlier

[3]Note that the central nucleus of the $Z \approx 138$, $N \approx 230$ island of stability of spherical hyperheavy nuclei does not really show $Z = 138$ shell gap in proton spectra (see discussion in Sec. V of Ref. [2]).

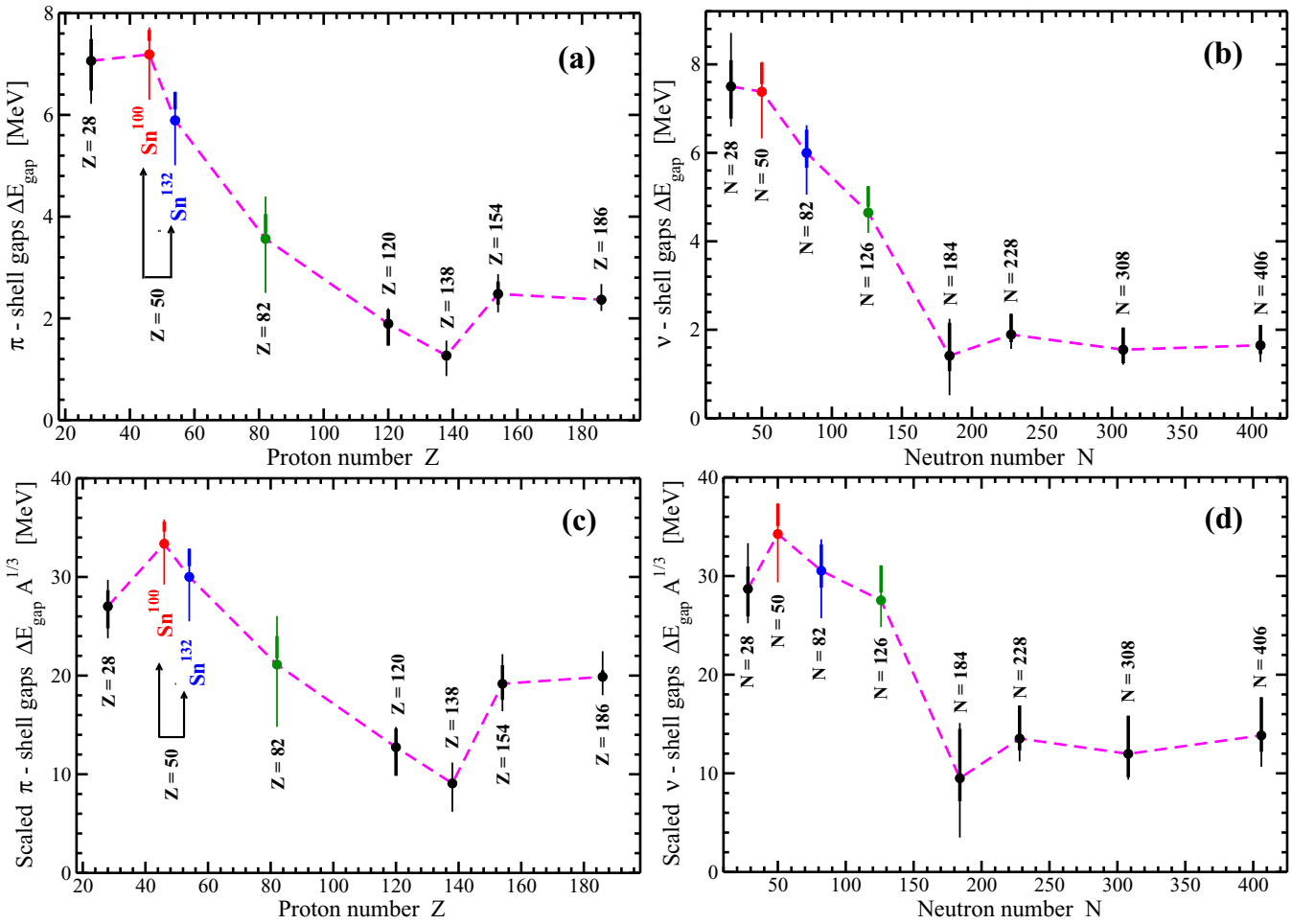

FIG. 3. [(a), (b)] Calculated proton (π) and neutron (ν) shell gaps $\Delta E_{\rm gap}$ in the doubly magic ^{58}Ni, ^{100,132}Sn, and ^{208}Pb nuclei and shell-closure superheavy ^{304}120 and hyperheavy ^{366}138, ^{462}154, and ^{592}186 nuclei. Note that last three nuclei are located in the centers of the islands of stability of spherical hyperheavy nuclei. Particle numbers corresponding to shell gaps are indicated. Ten most widely used CEDFs, namely, NL1 [31], NL3 [32], NL3* [33], FSUGold [34], DD-ME2 [35], DD-MEδ [36], DD-PC1 [22], PC-PK1 [37], PC-F1 [38], and TM1 [39] are employed in the calculations. The average (among the 10 used CEDFs) size of the shell gap is shown by a solid circle while the gaps obtained for individual functionals are summarized in Table I. Thin and thick vertical lines are used to show the spread of the sizes of the calculated shell gaps; the tops and bottoms of these lines correspond to the upper and lower shell gaps among the considered set of CEDFs. Thin lines show this spread for all employed CEDF's, while thick lines are used for the subset of four globally tested CEDFs (NL3*, DD-ME2, DD-PC1, and PC-PK1). [(c), (d)] The same as in panels (a) and (b) respectively, but with the sizes of the shell gaps and the spreads in their predictions scaled with mass factor $A^{\frac{1}{3}}$.

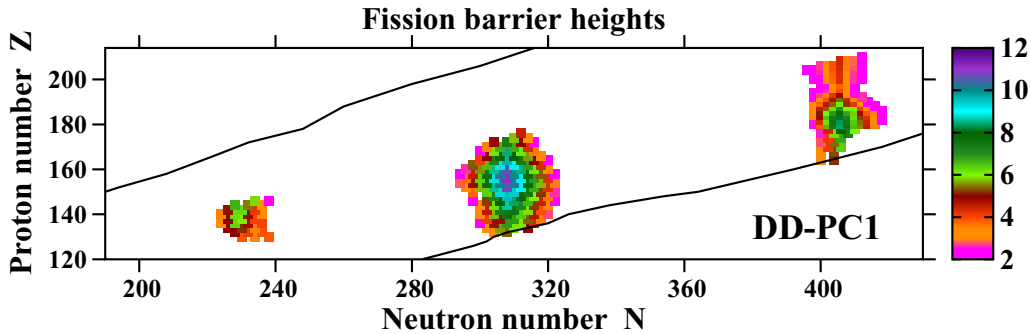

FIG. 4. The fission barrier heights E_B [in MeV] as a function of proton and neutron numbers. Only the nuclei with fission barriers higher than 2 MeV are shown. Partially based on the results presented in Fig. 6(a) of Ref. [1].

TABLE I. The heights of the fission barriers E_B and the sizes ΔE of spherical $N = 406$ ($\Delta E_{N=406}$) and $Z = 186$ ($\Delta E_{Z=186}$) shell gaps in the $^{592}186$ nucleus obtained with indicated CEDFs. The functionals are ordered in such a way that E_B is decreasing.

CEDF	E_B[MeV]	$\Delta E_{N=406}$ [MeV]	$\Delta E_{Z=186}$ [MeV]
FSUGold	10.66	1.84	2.17
DD-ME2	7.73	2.11	2.43
DD-MEδ	7.72	1.98	2.68
DD-PC1	7.59	1.93	2.45
PC-PK1	4.35	1.61	2.37
NL3	4.28	1.43	2.15
PC-F1	3.87	1.41	2.45
TM1	3.86	1.38	2.29
NL3*	3.59	1.45	2.37
NL1	1.27	1.27	2.34

published range of $Z = 120$–180 (see Fig. 6(a) in Ref. [1]) to the range of proton numbers from $Z = 120$ up to $Z = 210$. The value of the fission barrier height E_B is defined as the lowest value of the barriers located on the oblate and prolate sides with respect to spherical state in the deformation energy curves obtained in axial RHB calculations. One can see that the island of spherical hyperheavy nuclei previously labeled as the "$Z \approx 174, N \approx 410$ island" in Ref. [1] has been considerably extended up to $Z \approx 206$. In a given isotope chain of this island, the maximum of fission barriers heights is located at $N = 406$. The highest fission barriers with the heights between $\approx$7.5 and $\approx$8.5 MeV are found in the $Z = 186$, 184, 182, and 180 isotopic chains. They are higher than those obtained in the classical region of superheavy nuclei (see Ref. [24]). Based on these results for fission barriers and for the sizes of the $Z = 186, N = 406$ spherical shell gaps, we relabel this island as the "$Z \approx 186, N \approx 406$ island of spherical hyperheavy nuclei." The extension of upper boundary of nuclear landscape from $Z = 180$ to $Z = 210$ does not reveal other islands of spherical hyperheavy nuclei.

Similar to the results presented in Fig. 6 of Ref. [1], the size of the $Z \approx 186, N \approx 406$ island of spherical hyperheavy nuclei and the stability of the elements in it are expected to depend strongly on the employed functional. We have not attempted to map this region with other than DD-PC1 functionals but some insight on this issue can be obtained from the analysis of the heights of fission barrier E_B of the central nucleus ($^{592}186$) of this region calculated with different functionals. These results are summarized in Table I. The FSUGold and next three functionals (DD-ME2, DD-MEδ, and DD-PC1) produce the highest calculated fission barriers: at 10.66 MeV for FSUGold and clustered around $E_B \approx 7.7$ MeV for other three functionals. These barriers are higher than those produced in the covariant density functional theory (CDFT) framework in the classical region of superheavy nuclei (see Fig. 10 in Ref. [24]). These functionals are also expected to produce the island of spherical hyperheavy nuclei, which is comparable in size to that shown in Fig. 4. The next five functionals (PC-PK1, NL3, PC-F1, TM1, and NL3*) produce the cluster with $E_B \approx 4$ MeV (see Table I); this value is not far away from what is obtained in the $Z \approx 116, Z \approx 180$ region of superheavy nuclei (see Fig. 10 in Ref. [24]). For these functionals, the $Z \approx 186, N \approx 406$ island of stability of spherical hyperheavy nuclei is expected to be substantially smaller than the one shown in Fig. 4. Finally, the lowest fission barrier is produced by the NL1 functional; its value indicates the instability of spherical hyperheavy nuclei. However, the predictions of this functional have to be considered as least reliable because of well-known problems in its isovector properties (see Ref. [32]).

The difference in the predictions of E_B is in part related to the fact that the first group of functionals predicts the $Z = 186$ and $N = 406$ shell gaps, which are on average larger by $\approx$0.1 MeV and $\approx$0.5 MeV, respectively, than those produced by the second group of CEDFs (see Table I). Note also that the nuclear matter properties and the density dependence are substantially better defined for density-dependent (DD*) functionals as compared with nonlinear (NL* and TM1) and point-coupling (PC-PK1 and PC-F1) ones [25]. As a consequence, in general, they are expected to perform better for large extrapolations from known regions.

Note that the axial RHB calculations for deformation energy curves in the vicinity of spherical minimum indicate nearly symmetric barriers with saddles at $\beta_2 \approx \pm 0.2$ [similar to Fig. 17(b) below]. The experience in actinides and superheavy nuclei tells us that octupole deformation in fission barrier area typically does not develop for such low deformations [4,26,44] [corresponding to inner fission barrier in actinides and superheavy nuclei] and this result has been confirmed in octupole deformed RHB calculations with CEDF DD-PC1 for spherical minimum of several hyperheavy nuclei in Ref. [2]. The results presented in Fig. 5 for the $^{592}186$ nucleus are in line with these expectations; the saddle of fission barrier is located at $\beta_3 = 0.0$ and octupole deformation does not affect the spherical minimum in the calculations with DD-PC1 and NL3* functionals.

The analysis of Ref. [2] indicates that the impact of triaxial deformation on the fission barriers around the spherical minima is relatively modest. This is the consequence of the topology of potential energy surfaces, which is similar to those of volcanos (see Fig. 6). The central area around the spherical minimum is similar to a caldera, the rim of which is represented by the fission barrier. The area beyond the rim (fission barrier) is a steep downslope as a function of quadrupole deformation β_2. The saddles of axial fission barriers (on oblate and prolate sides of spherical minimum) are located at modest quadrupole deformation of $\beta_2 \approx 0.2$. As a result, the distance between these two saddles in the (β_2, γ) plane plane is relatively small, so that large changes in binding energy due to triaxiality for nearly constant β_2 values could not develop. As a consequence, the lowest fission barrier around spherical minimum obtained in axial RHB calculations is a good approximation to the barrier obtained in the triaxial relativistic Hartree-Bogoliubov (TRHB) calculations. For example, this is a case in the calculations with CEDF DD-PC1 [see Fig. 6(a)]. Even if the saddle of fission barrier is located at $\gamma \neq 0^\circ$ and $\gamma \neq 60^\circ$, the energy lowering in fission barrier height as compared with the lowest fission barrier at these γ values is rather modest. For example, in the calculations with the NL3* functional, the saddle of the fission barrier, located

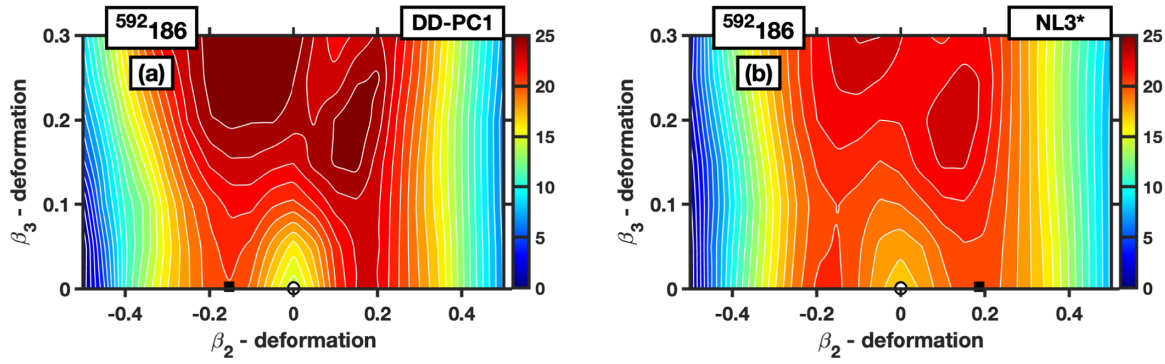

FIG. 5. Potential energy surfaces of the $^{592}186$ nucleus obtained in the reflection asymmetric (octupole deformed) RHB calculations with indicated CEDFs. The energy difference between two neighboring equipotential lines is equal to 1.0 MeV. Spherical minimum is indicated by a circle and the saddle point of the barrier around spherical minimum by solid black square. The color maps show the excitation energies (in MeV) with respect to the energy of the deformation point with largest (in absolute value) binding energy. The calculations are performed with $N_F = 20$. Note that the topology of potential energy surfaces is almost the same in the calculations with $N_F = 20$ and $N_F = 26$. Thus, to save computational time these figures are plotted with $N_F = 20$.

at $\gamma = 22^\circ$, is lower than the fission barrier at $\gamma = 0^\circ$ by only 50 keV [see Fig. 6(b)]. Note also that the TRHB results clearly indicate that spherical minimum of the nucleus under study is relatively stable with respect to triaxial distortions.

Although the detailed studies have only been performed with two functionals, representing one of the highest (DD-PC1) and one of the lowest (NL3*) fission barriers obtained in the calculations (see Table I), it is reasonable to expect that similar situation will hold also for other functionals. This is because of the similarity of the underlying shell structure. Thus, one conclude that the impact of triaxiality and octupole deformation on E_B of spherical hyperheavy nuclei is either very small or nonexistent (see also the discussion in Refs. [1,2]).

The density distributions at spherical shape for the nuclei representing the centers of the islands of spherical hyperheavy nuclei have been compared and discussed in Sec. IV of Ref. [2]. However, the $Z \approx 186$, $N \approx 406$ island (and, in particular, doubly magic $^{592}186$ nucleus corresponding to large shell gaps at $Z = 186$ and $N = 406$) has not been completely covered in that study because of the restriction to the $Z \leqslant 180$ nuclei. To fill this gap in our knowledge, Fig. 7 compares proton and neutron density distributions of the $^{584}174$ nucleus (studied in Ref. [2]) with those of doubly magic $^{592}186$ one. Neutron densities of these two nuclei are very similar; they are slightly larger for the $^{584}174$ nucleus because of the occupation of the $2j_{13/2}$ orbitals by four additional neutrons. The differences are more visible for proton densities because 12 additional protons in the doubly magic $^{592}186$ nucleus (eight in the $2g_{7/2}$ and four in $1j_{13/2}$ orbitals) occupy the orbitals which fill the density either in surface region (the $1j_{13/2}$ orbitals) or in-between central and surface regions (the $2g_{7/2}$ orbitals) (see Ref. [45]). The increase of the Coulomb repulsion in the $Z = 186$ nucleus as compared with the $Z = 174$ one also plays a role in an enhancement of proton density near the surface. As a consequence, the semibubble structure

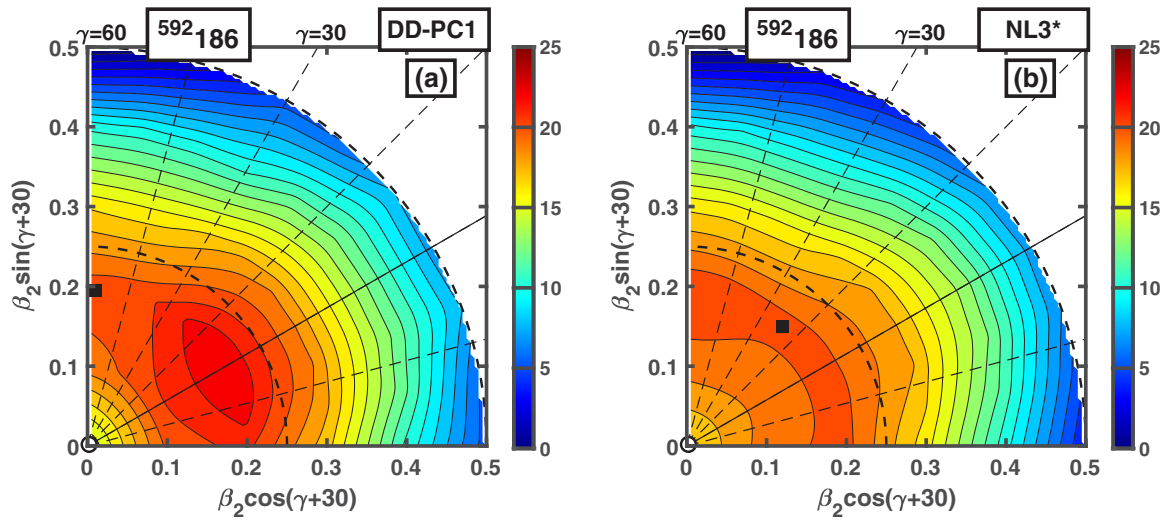

FIG. 6. The same as in Fig. 5 but for potential energy surfaces obtained in triaxial RHB calculations.

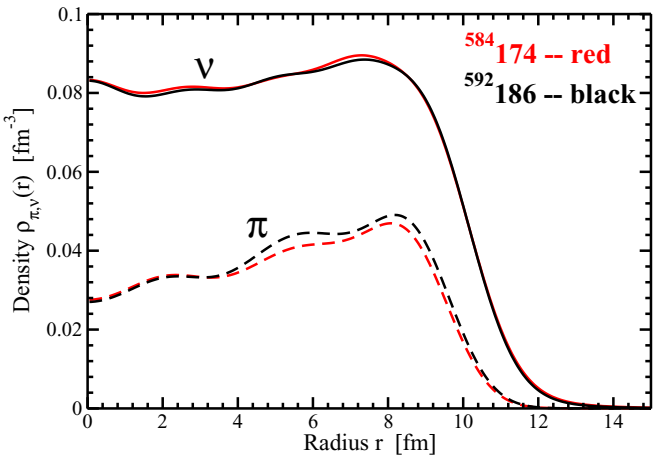

FIG. 7. Proton and neutron densities of the $^{584}174$ and $^{592}186$ nuclei. The figure is based on the results of spherical RHB calculations.

becomes more pronounced in the proton densities of the $^{592}186$ nucleus as compared with the $^{584}174$ one.

IV. TOROIDAL NUCLEI

A. Distribution of shapes of toroidal nuclei across the nuclear landscape

In our calculations, the truncation of basis is performed in such a way that all states belonging to the major shells up to N_F fermionic shells for the Dirac spinors are taken into account. Accurate calculations of LEMAS require extremely large fermionic basis and its size, defined by N_F, increases with the raise of proton and neutron numbers (see discussion in Sec. III of Ref. [2]). As a result, the β_2 values (and, thus, respective density distributions) of the lowest in energy toroidal states have only been partially mapped in the $Z = 122$–138 region (see Fig. 3 in Ref. [1]) in the axial RHB calculations with $N_F = 26$. For higher Z nuclei, existing calculations only confirm that the lowest in energy solutions have always toroidal shapes (see the discussion of Fig. 3 in Ref. [2]) but do not provide accurate β_2 values.

To fill this gap in our knowledge, additional calculations are performed in the $N_F = 30$ basis which provides quite accurate description of toroidal shapes in the $Z \geqslant 140$ hyperheavy nuclei (see Sec. III in Ref. [2]). Such calculations are extremely time-consuming even in axial RHB framework and thus they are carried out only for restricted set of nuclei displayed in Fig. 8. These are $Z = 136$, 146, 156, 166, and 176 nuclei. Apart of few regions, the calculations are performed in step of $\Delta N = 10$ to save computational time. Despite these limitations, they allow us to understand the general features of the distribution of toroidal shapes as well as the evolution of underlying single-particle structure across the nuclear chart.

The results of these calculations are presented in Fig. 8. To facilitate the discussion, we are using here the definitions of tori as *thin* and *fat* employed in the physics of toroidal liquid droplets [46]. Large (small) ratios of the radius R of toroid (called the "major radius" in some publications; see, for example, Ref. [5]) to the radius d of its tube (called the "minor radius" in Ref. [5]) correspond to thin (fat) tori. The lowest β_2 values ($\beta_2 \approx -2.2$) are obtained in the $Z \approx 136$, $N \approx 206$ region (see Fig. 8) and these nuclei can be defined as fat toroidal nuclei because of small aspect ratio R/d. The absolute β_2 values increase upon moving away from this region. Especially large values of $|\beta_2|$ are obtained in proton-rich

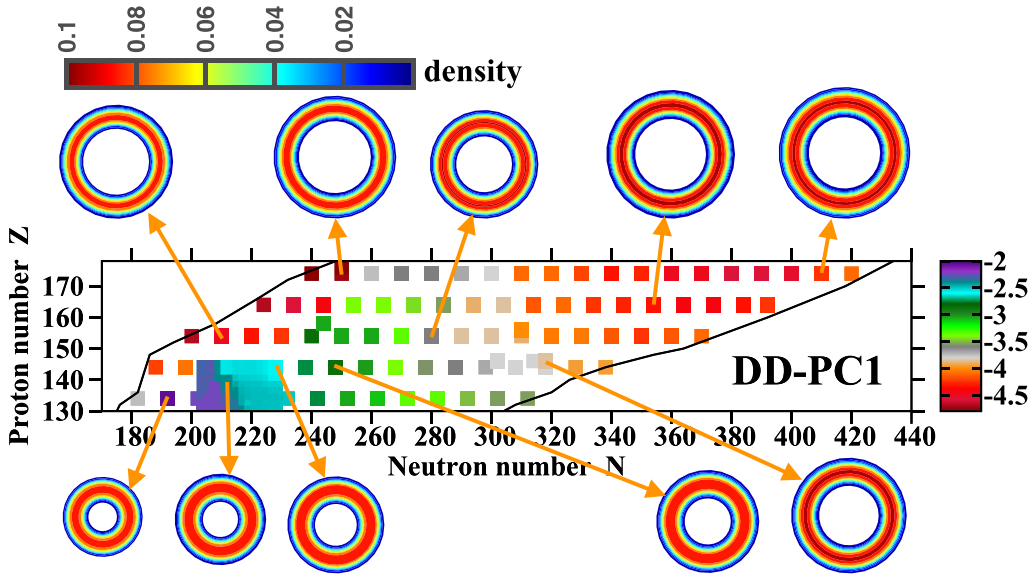

FIG. 8. Proton β_2 values (see color map on right) of the lowest in energy solutions of selected set of nuclei (see text for details). Solid black lines indicate two-proton and two-neutron drip lines. Neutron density distributions of some nuclei are shown: Orange arrows are used to indicate these nuclei. The same color map (shown in the upper left corner) as the one used in Figs. 1 and 9 is employed here for the densities. The density color map starts at $\rho_n = 0.005$ fm^{-3} and shows the densities in fm^{-3}. The density of the $^{348}138$ nucleus is used here as a reference (see Fig. 9 for its actual geometrical size) with respect of which the geometrical sizes of the density distributions in other nuclei are normalized.

nuclei with $Z > 140$ in the vicinity of the two-proton drip line. These toroidal shapes are characterized by very large radius of the torus and small radius of the torus tube and thus these nuclei are described as thin toroidal nuclei. Slightly smaller values of $|\beta_2|$ are seen in neutron-rich $N \geqslant 310$ nuclei. The aspect ratios R/d for these nuclei are slightly smaller as compared with the ones in proton-rich nuclei but these nuclei are still the representatives of thin toroidal nuclei. Remaining nuclei shown by cyan, dark and light green, and gray colors in Fig. 8 are characterized by β_2 ranging from -2.5 to -3.7. A general trend of the increase of torus radius R and the aspect ratio R/d with increasing proton number is seen in Fig. 8. It is a consequence of Coulomb repulsion: Toroidal shapes provide less compact distribution of charge as compared with spherical ones and thus the Coulomb energy is substantially reduced for toroidal shapes as compared with spherical ones (see discussion in Sec. XII in Ref. [2])). The increase of proton number requires the increase of torus radius in order to minimize the Coulomb energy by creating less compact distribution of charge. Observed features in the distribution of toroidal shapes, which are the result of the competition of different energy minima similar to the minima A and B shown in Fig. 1 (see also Fig. 16 in Ref. [2]), have roots in the underlying shell structure of toroidal hyperheavy nuclei (see Sec. IV B).

To get a better understanding of the relative properties of proton and neutron density distributions, we compare them in Fig. 9 for the $^{348}138$ and $^{466}156$ nuclei. Similar to the situation at spherical shape (see, for example, Fig. 7), the maximum of proton density distribution $\rho_\pi^{\max}$ is significantly smaller ($\rho_\pi^{\max} \approx \frac{2}{3}\rho_\nu^{\max}$) than the neutron one $\rho_\nu^{\max}$ and those maxima do not necessary appear at the same distance from the center of toroid. The outer edges of the proton and neutron density distributions appear at approximately the same distances from the center of toroid. However, the diameter of the hole in the center of proton density distribution is visibly larger than the one in the case of neutrons. This is most likely the consequence of the Coulomb repulsion acting on protons. Thus, the diameter of toroid tube is smaller in the case of protons as compared with the one for neutrons. Note also that the density distribution in toroid tube is not necessary symmetric with respect of its geometrical axis of symmetry; this is especially visible in the case of proton density distributions presented in Figs. 9(b) and 9(d). Detailed analysis reveals that this is a consequence of the occupation of the single-particle orbitals characterized by different spatial distributions of the single-particle densities.

Because of the presence of well-pronounced minima (similar to the minimum D in Fig. 1), the present axial RHB calculations in extremely large basis confirm for the first time the stability of toroidal $Z \geqslant 140$ nuclei shown in Fig. 8 with respect of so-called breathing deformations. The breathing deformation [5] preserves the azimuthal symmetry of the torus and it is defined by the radius of torus and the radius of its tube. In our calculations, this type of deformation is related to the β_2 values (see discussion in Ref. [1]). This result is clearly different as compared with the ones obtained for classical uncharged toroidal liquid droplets, which are unstable with respect of shrinking instabilities [20,46,47]. Because of surface tension, such droplet starts from toroidal shape but then gradually shrinks by closing its interior hole and transforms into spherical droplet [20,46,47]. In atomic nuclei, this shrinking instability is counteracted by the Coulomb force: The transition to a more compact spherical configuration leads to a substantial increase of the Coulomb energy and thus it is not energetically favored in hyperheavy nuclei [2].

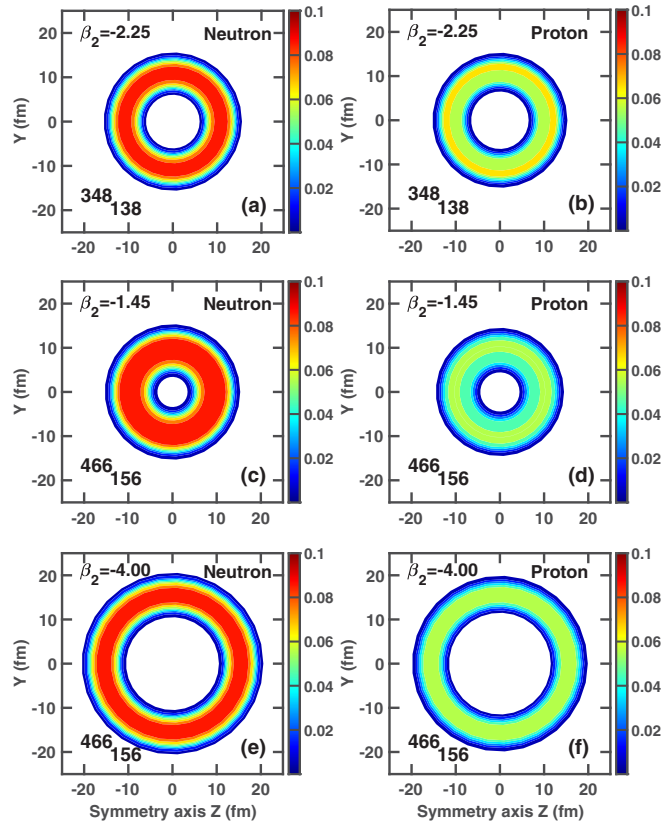

FIG. 9. Neutron ρ_ν (left column) and proton ρ_π (right column) density distributions of toroidal configurations in the $\beta_2 = -2.25$ minimum of the $^{348}138$ nucleus and in the minima B and A of the $^{466}156$ nucleus (see Fig. 1).

Another class of potential instabilities of toroidal nuclei is related to so-called sausage deformations [5]: They make a torus thicker in one section(s) and thinner in another section(s). This class of the instabilities is much more difficult to describe in the density functional theories since their consideration requires, in general, symmetry-unrestricted computer codes. This fact, combined with the requirement for extremely large basis in high-Z systems, makes this problem numerically intractable with existing computer codes for absolute majority of toroidal nuclei. The only exception are fat toroidal nuclei located in the $Z \approx 136, N \approx 210$ region for which (as illustrated by the examples of the $^{354}134$ and $^{348}138$ nuclei discussed in Refs. [1,2]) the calculations for even-multipole sausage deformations within the triaxial relativistic mean field (RMF) +BCS codes are possible [1]. However, even such calculations are extremely time-consuming and can be performed only for a few nuclei.

In such a situation, it is useful to get some insight from the studies of classical liquid droplets. Thin toroidal droplets exhibit Plateau-Rayleigh instabilities: When the outer circumferences of toroid is equal to an integer (n) times of the wavelength λ_c of unstable mode, the toroidal droplet will eventually fission into n spherical droplets [46] (see also Ref. [48] for the results obtained for liquid toroidal droplets suspended in another liquid). Note that in classical toroidal liquid droplets the Plateau-Rayleigh instability disappears for sufficiently fat tori ($R/d \leqslant 2$) while the shrinking mode is present for all aspect ratios [46]. These features have been confirmed in experimental studies of stability of both toroidal droplets in a viscous liquid [49] as well as melted polymer rings [50]. The instability with respect of so-called sausage deformations [5] in nuclear physics leading to multifragmentation[4] is an analog of the Plateau-Rayleigh instabilities. Thus, these results suggest that such instabilities are less important for fat toroidal nuclei [characterized by low (in absolute sense) values of $\beta_2 > -2.5$ and located in the $Z \approx 134, N \approx 210$ region (see Fig. 8)] but become more critical (and probably fatal) for thin toroidal nuclei characterized by large (in absolute sense) values of β_2. The latter type of nuclei become dominant both with increasing proton number Z and in proton- and neutron-rich nuclei (see Fig. 8). The former suggestion is in line with the results of triaxial RMF+BCS calculations for the $^{354}134$ and $^{348}138$ nuclei, which have 4.4- and 8.54-MeV fission barriers for nonaxial distortions, respectively (see Ref. [1]).

However, it is necessary to recognize that fully quantum mechanical calculations based on the density functional theory are needed for establishing the stability of toroidal nuclei with respect of sausage deformations. Toroidal liquid droplets have a uniform density and the tube of torus has a cylindrical form [46]. In contrast, the density functional theory (DFT) calculations paint a much more complicated picture. First, the density rapidly changes across the tube of the torus with considerable mismatch between proton and neutron densities (see Fig. 9 in the present paper, Figs. 2(c) and 2(d) in Ref. [1], and Fig. 9 in Ref. [51]), which are defined by the occupation of underlying proton and neutron single-particle orbitals. The description of such a situation on the level of liquid-drop model would require the model based on two (proton and neutron) fluids with the specification of functional dependencies of their densities on the position in the tube of the torus. Second, not in all cases is the tube of the torus represented by a perfect cylinder (see Fig. 2 in Ref. [2]). This may lead to an enhanced stability against sausage deformations since experimental studies of toroidal liquid droplets show that oblong cross section of the torus tube suppresses Plateau-Rayleigh instabilities as compared with circular one [47]. Because of above-mentioned reasons, the analysis of Ref. [5] indicating the instability of toroidal nuclei with respect of sausage deformations in the liquid drop model should not be taken at face value. Note also that this analysis considers only the nuclei with $Z < 120$ in which toroidal shapes are formed at high excitation energies with respect to the ground states while the toroidal shapes in the majority of hyperheavy nuclei are expected to be the ground states. Moreover, the quantum shell effects can counterbalance the potential instabilities toward sausage deformations at some combinations of proton and neutron numbers and deformations [1,5].

[4]In this context, it would be interesting to see whether the observed multifragmentation of high-spin configurations of ^{28}Si into seven α particles [19] represents the analog of Plateau-Rayleigh instabilities of toroidal droplets in nuclear physics.

B. Shell structure of toroidal hyperheavy nuclei

It is well known that the presence of large gaps in proton and neutron single-particle energies leads to an extra stability of nuclear systems. So far, the analysis of toroidal shell structure at spin $I = 0$ has been performed in light nuclei [5,51], in the intermediate-mass region nuclei [52], and in superheavy $Z \approx 120$ nuclei [15,17]. Such an analysis was based either on phenomenological toroidal single-particle potential (see Refs. [5,51,52]) or on Skyrme DFT calculations (see Refs. [15,17,51]). Large gaps in the single-particle energies have been found at toroidal shapes in all these regions. For example, in light nuclei these energy gaps give rise to "toroidal shells" at "magic" nucleon numbers $N = 2(2m + 1)$ with m being an integer satisfying the condition $m \geqslant 1$ [5]. The extra stability associated with toroidal shells leads to local energy minima at toroidal shapes in many nuclei either at spin zero [5,53] or in some high-spin isomer states [51]. However, in all these nuclei such minima are located at high excitation energies with respect to ellipsoidal-like ground state.

However, the situation changes in hyperheavy nuclei in which the ground states are expected to have toroidal shapes. Thus, it is very important to investigate shell structures of toroidal hyperheavy nuclei. In particular, it would be interesting to see whether there are large shell gaps or reduced density of the single-particle states at specific particle numbers which could provide extra stability with respect to potential instabilities originating from sausage deformations. One should also remember that even if hyperheavy nuclei are unstable with respect to sausage deformations in the liquid drop model, they can be stabilized by quantum shell corrections. The best known examples of such a situation are superheavy nuclei: They are unstable in the liquid drop model but are relatively stable in a fully quantum mechanical picture which includes shell corrections [54,55].

The analysis presented in Sec. IV A suggests that it is more likely to get potentially stable toroidal nuclei when their shapes in corresponding minima are characterized by small absolute β_2 values (or small aspect ratio R/d). The toroidal $^{354}134$ and $^{348}138$ nuclei are representative cases of such shapes (see Fig. 1 in the Supplemental Material to Ref. [1] and Fig. 19 in Ref. [2]). Triaxial RMF+BCS calculations of Refs. [1,2] suggest that these two nuclei are expected to be relatively stable with respect to nonaxial distortions (even-multipole sausage deformations) with calculated fission barriers being equal to 4.4 and 8.54 MeV, respectively. Enhanced stability of the $^{348}138$ nucleus is a reason why we start the analysis of toroidal shell structure from this nucleus, which is characterized by moderately compact toroidal shapes [see Figs. 9(a) and 9(b)]. We also consider toroidal shell

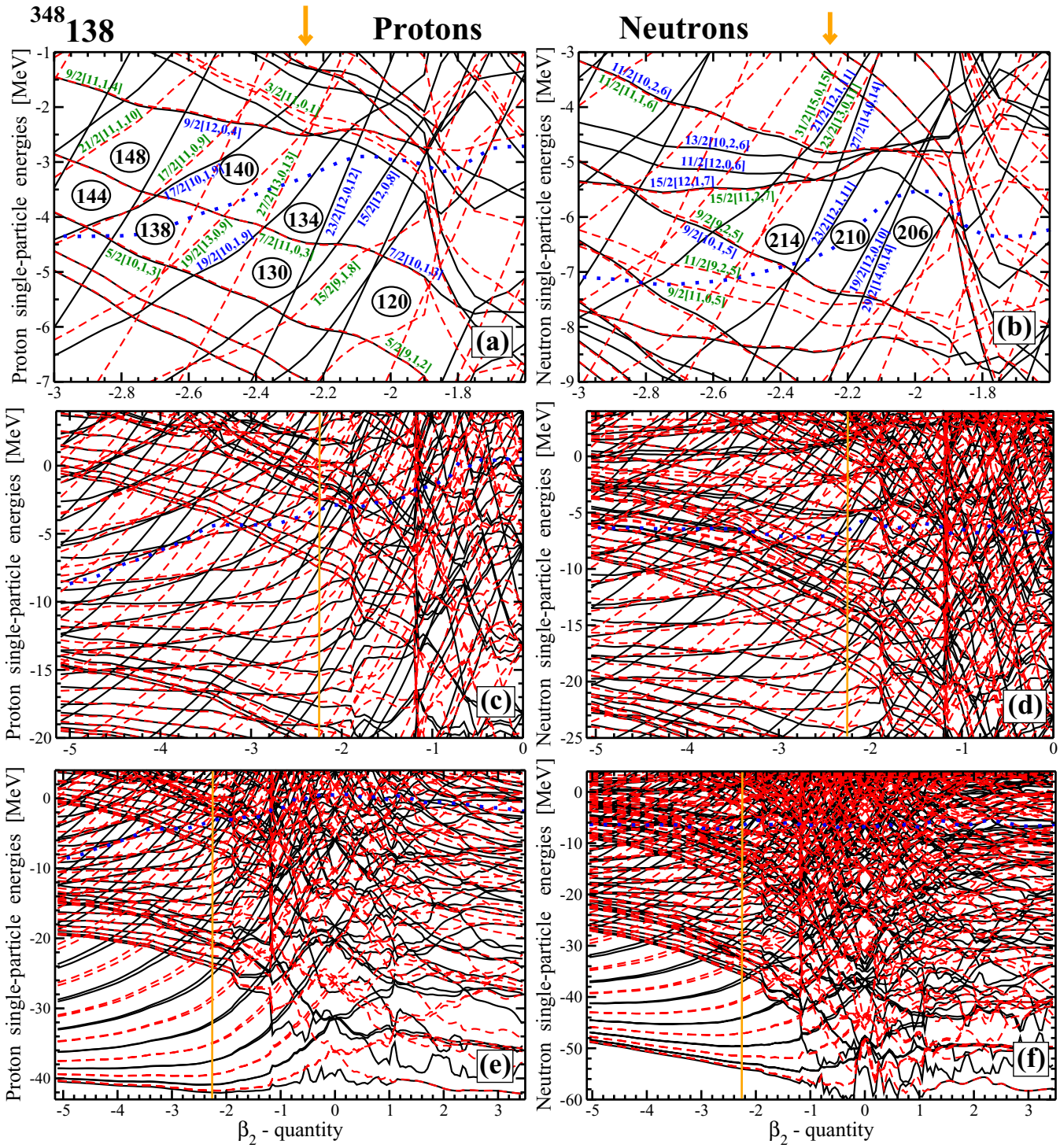

FIG. 10. Proton and neutron single-particle energies, i.e., the diagonal elements of the single-particle Hamiltonian h in the canonical basis [29], for the lowest in total energy solution in the $^{348}138$ nucleus calculated as a function of the β_2 quantity. Black solid and red dashed lines are used for positive- and negative-parity states, respectively. The dominant components $\Omega[N, n_z, \Lambda]$ of the wave functions (as calculated at LEMAS) are shown by blue and green colors for the positive- and negative-parity orbitals, respectively. The energies E_F of the respective Fermi levels are shown by blue dotted lines. The vertical orange lines and orange arrows are drawn at the β_2 value corresponding to LEMAS. Shell gaps are indicated by encircled numbers.

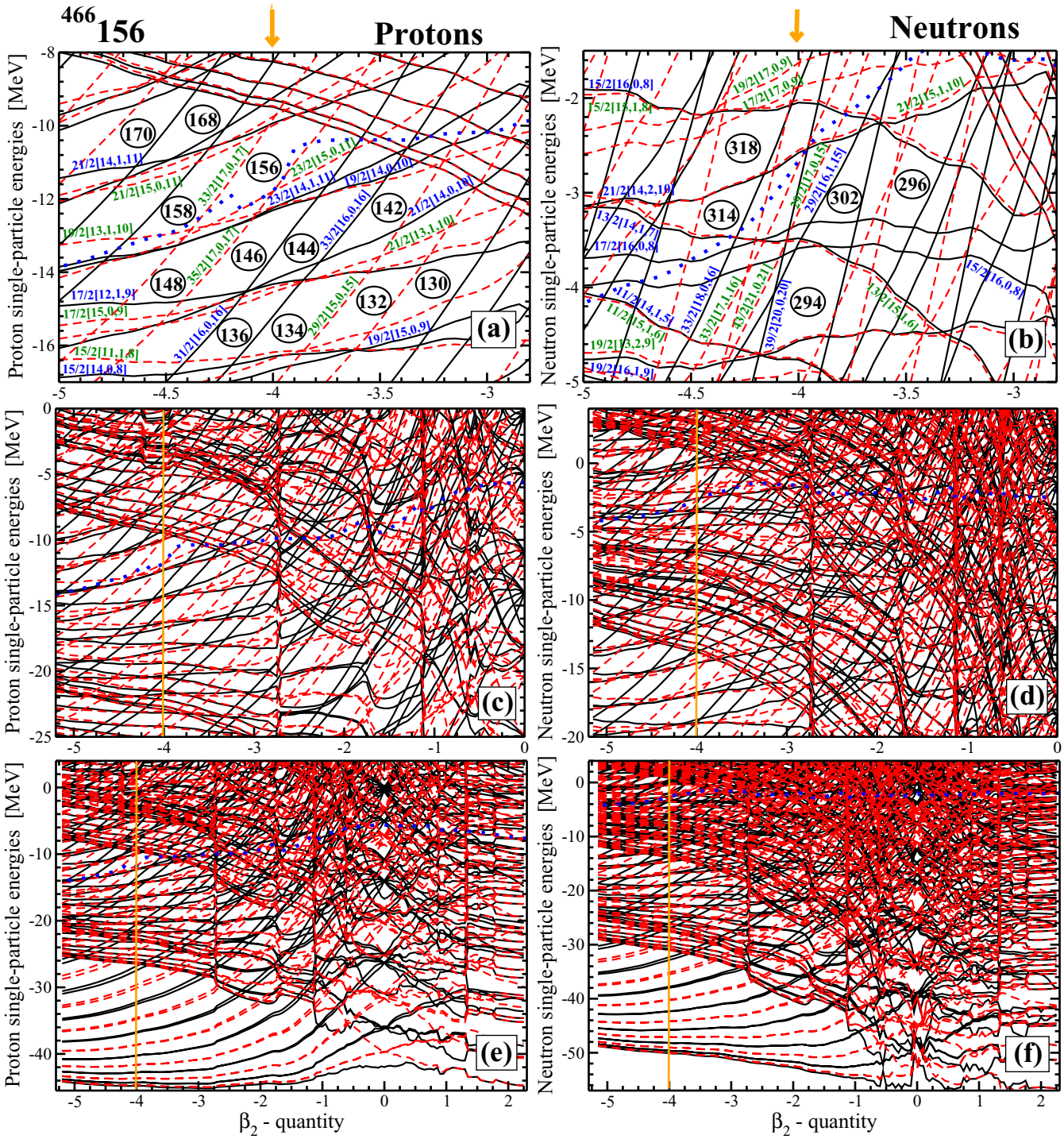

FIG. 11. The same as Fig. 10 but for the $^{466}156$ nucleus.

structure in the $^{466}156$ nucleus. The LEMAS of this nucleus is characterized by noncompact toroidal shapes with large R/d aspect ratio [see Figs. 9(e) and 9(f)], but there is also an excited minimum B (see Fig. 1) which is characterized by very compact toroidal shapes with very small holes in the centers [see Figs. 9(c) and 9(d)].

The Nilsson diagrams for these nuclei are shown in Figs. 10 and 11. In order to illustrate the differences between shell structures of toroidal and ellipsoidal-like nuclei, bottom panels display proton and neutron single-particle states in the very large energy and β_2 ranges. They are shown from the bottom of respective potentials up to 4 MeV energy above the continuum threshold and from $\beta_2 = -5.1$, corresponding to toroidal nuclei with large R/d aspect ratio, up to $\beta_2 = +3.5$ in the $^{348}138$ nucleus and up to $\beta_2 = 2.25$ in the $^{466}156$ nuclei. These large positive β_2 values correspond to prefissioning

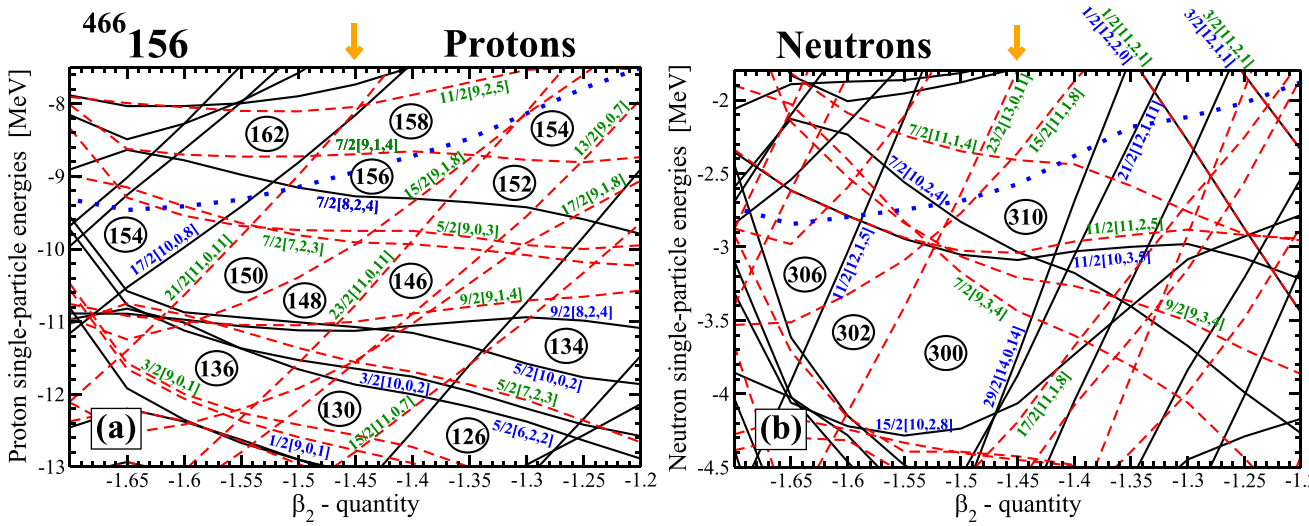

FIG. 12. The same as Fig. 11 but for the single-particle states active in the vicinity of the Fermi levels corresponding to the minimum B of Fig. 1.

configurations with well-pronounced necks (see, for example, density distribution at the position F of Fig. 1). Middle and top panels of Figs. 10 and 11 as well as Fig. 12 show the regions of interest in an enlarged scale. The analysis of these figures reveals the general features which are discussed below.

Toroidal shell structure (especially the one for the shapes with large R/d aspect ratio) has much more pronounced regular features as compared with the shell structure of ellipsoidal-like shapes in the range of the β_2 values from ≈ -1.15 up to ≈ 1.5 which looks quite chaotic for deformed shapes [see Figs. 10(e), 10(f), 11(e), and 11(f)]. At higher β_2 values, typical features of shell structure of two-center shell model (see, for example, Ref. [56]) are seen.

The bunching of the pairs of the orbitals of the same parity with dominant structure of $\Omega[N, n_z, \Lambda]$ and $(\Omega+1)[N, n_z, \Lambda]$ with $N \geqslant 9$ and $n_z = 0$ (see Table II)[5] leads to the appearance of toroidal shell gaps at particle numbers 6, 10, 14, 18, 22, 26, 30, 34, 38, 42, and 46 at the bottom of proton and neutron potentials (see Fig. 13). These gaps exist in a large range of the β_2 values; this is contrary to the case of shell gaps for ellipsoid-like shapes which are localized in deformation. They are also consistent with the ones obtained in the study of toroidal shapes in light nuclei within toroidal harmonic oscillator shell model[6] and Skyrme DFT (see Figs. 1, 5, and 6 in Ref. [51] and Fig. 12 in Ref. [5]). The energies of these pairs of orbitals generally decrease with increasing the absolute value of β_2; the only exception from this rule are several lowest pairs of orbitals located at the bottom of neutron and proton potentials (see Fig. 13). Note that the pairs of the orbitals with dominant structure of $\Omega[N, n_z, \Lambda]$ and $(\Omega+1)[N, n_z, \Lambda]$ are almost near degenerate in energy at the bottom of potential and that this near-degeneracy increases with increasing absolute value of β_2. There is also an alternation of the pairs of the states with positive and negative parities with increasing energy (see Fig. 13). These features of the shell structure dominate the physics of toroidal shapes in light to medium-mass nuclei (see Refs. [5,51]).

The general features of the pairs of orbitals with dominant structure of $\Omega[N, n_z, \Lambda]$ and $(\Omega+1)[N, n_z, \Lambda]$ with $n_z = 0$ changes drastically in the energy ranges between -20 and 0

TABLE II. The dominant components of the wave functions of nearly degenerate pairs of the single-particle states of same parity indicated by the letters in Fig. 13. They are defined at the β_2 value corresponding to LEMAS. The states forming the pair are shown in the columns labeled as "first state" and "second state."

	First state	Second state
a	1/2[9,0,1]	3/2[9,0,1]
b	3/2[10,0,2]	5/2[10,0,2]
c	5/2[9,0,3]	7/2[9,0,3]
d	7/2[10,0,4]	9/2[10,0,4]
e	9/2[9,0,5]	11/2[9,0,5]
f	11/2[10,0,6]	13/2[10,0,6]
g	13/2[11,0,7]	15/2[11,0,7]
h	15/2[10,0,8]	17/2[10,0,8]
i	17/2[11,0,9]	19/2[11,0,9]
j	19/2[12,0,10]	21/2[12,0,10]
k	21/2[13,0,11]	23/2[13,0,11]
l	23/2[12,0,12]	25/2[14,1,12]

[5]The only exception is the last pair of the states shown in Table II for which the second state has $n_z = 1$.

[6]This type of the model has been described before either as a shell model based on radially displaced harmonic oscillator potential [5,51] or a harmonic oscillator toroidal shell model [52]. We abbreviate it here as toroidal harmonic oscillator shell model in order to stress that the basis of it is formed by the eigenvectors of radially displaced (toroidal) harmonic oscillator potential and that in this respect it differs from the standard shell model which uses a traditional harmonic oscillator for basis set expansion.

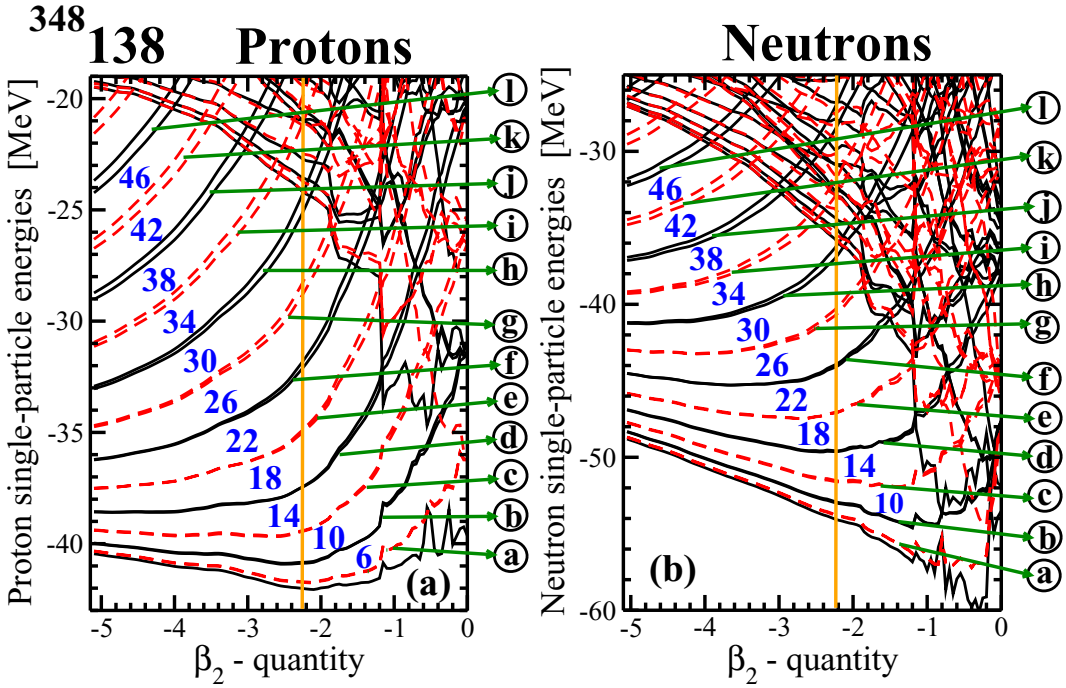

FIG. 13. The same as Fig. 10 but for the single-particle states located in the bottom part of nucleonic potential and in the β_2 range from -5.1 up to 0.0. Toroidal shell gaps are shown by bold blue numbers. Encircled letters and green arrows are used to indicate the pairs of the single-particle states which are almost degenerate in energy. The structure of these states are shown in Table II.

MeV for protons and between -25 and 0 MeV for neutrons (see Figs. 10, 11, and 14) for $\beta_2 \leqslant -1.8$. First, their energies decrease almost linearly with increasing absolute value of β_2. Second, there is a periodic pattern in the change of the orbitals: With increasing energy, two positive-parity orbitals are followed by two negative-parity orbitals, then by two positive-parity orbitals, and so on. Third, these orbitals form the grating-like structure with almost equidistant energy spacings between them.

In the same energy range as discussed in the previous paragraph, there are other single-particle structures dictated by the symmetries of the toroid. These are almost degenerate in energy single-particle states of opposite parity (see Figs. 14, 10, and 11) with dominant structures of the wave functions given by $\Omega[N, n_z, \Lambda]$ and $\Omega[N', n'_z, \Lambda']$, where the conditions $N' = N \pm 1$, $|\Lambda' - \Lambda| = 0$ or 1 and $|n'_z - n_z| = 0$ or 1 are typically satified (see Table III). These states change their energy very slowly when the β_2 value is varied. Note that such pairs of the states are also present in the Skyrme DFT calculations of toroidal shapes in the $^{304}120$ nucleus (see Figs. 3 and 4 in Ref. [17]).

The presence of the two types of the single-particle states discussed in the previous two items is mostly responsible for the shell structure and shell gaps in the intermediate energy range of proton and neutron potentials. This leads to the existence of many gaps in the single-particle spectra which are quite large. These are proton $Z = 120$, 130, 134, 138, 140, 144, and 148 shell gaps with typical size of approximately 1 MeV and neutron $N = 206$, 210, and

TABLE III. The dominant components of the wave functions of the pairs of proton and neutron single-particle states of opposite parity which are almost degenerate in energy. The states forming the pair are shown in the columns labeled as "parity= +" and "parity= −." These pairs are indicated in Fig. 14. Note that the dominant components of the wave functions are defined at the β_2 value corresponding to LEMAS.

	Neutron(ν)		Proton(π)	
	2	3	4	5
1	Parity= +	Parity= −	Parity= +	Parity= −
a	1/2[8,0,0]	1/2[9,0,1]	1/2[8,0,0]	1/2[9,0,1]
b	3/2[8,0,2]	3/2[9,0,1]	3/2[6,1,1]	3/2[9,0,1]
c	1/2[6,1,1]	1/2[7,1,0]	5/2[8,0,2]	5/2[7,1,2]
d	13/2[10,0,6]	13/2[9,1,6]	7/2[8,1,3]	7/2[9,0,3]
e	13/2[8,1,7]	13/2[11,0,7]	1/2[6,1,1]	1/2[7,1,0]
f	1/2[10,1,1]	1/2[9,1,0]	3/2[6,1,1]	3/2[7,1,2]
g	3/2[10,1,1]	3/2[11,0,1]	9/2[10,0,4]	9/2[7,1,4]
h	5/2[10,1,3]	5/2[9,1,2]	11/2[8,1,5]	11/2[9,0,5]
i	7/2[10,1,3]	7/2[11,0,3]	13/2[10,0,6]	13/2[9,1,6]
j	5/2[10,1,3]	5/2[9,2,3]	11/2[10,0,6]	11/2[9,1,6]
k	7/2[8,2,4]	7/2[11,1,4]	13/2[8,1,7]	13/2[11,0,7]
l	13/2[10,2,6]	13/2[11,1,6]	1/2[10,1,1]	1/2[9,1,0]
m	9/2[10,1,5]	9/2[9,2,5]	3/2[10,1,1]	3/2[11,0,1]
n	15/2[12,1,7]	15/2[11,2,7]	5/2[10,1,3]	5/2[9,1,2]
o	11/2[10,2,6]	11/2[11,1,6]	7/2[10,1,3]	7/2[11,0,3]
p			9/2[12,0,4]	9/2[11,1,4]
q			1/2[10,1,1]	1/2[7,2,1]
r			3/2[8,2,2]	3/2[9,1,2]

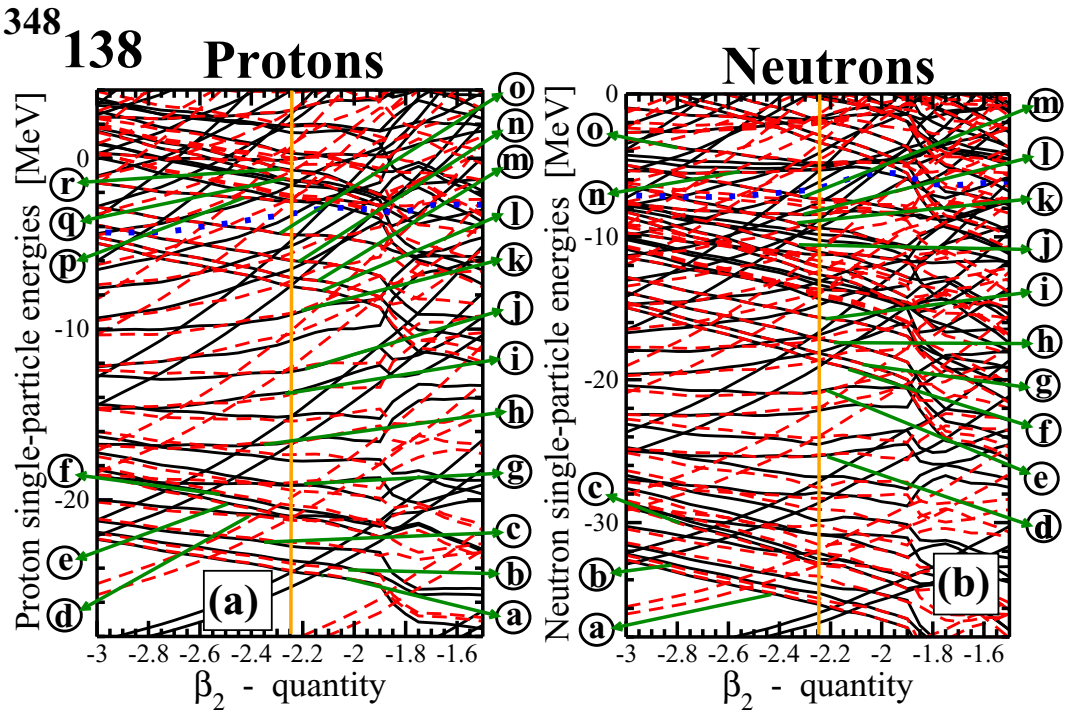

FIG. 14. The same as Fig. 10 but for the single-particle states located in the intermediate energy range of nucleonic potential of the $^{348}138$ nucleus and in the β_2 range from -3.0 up to -1.5. Encircled letters and green arrows are used to indicate the pairs of single-particle states of opposite parity which are almost degenerate in energy. The structure of these states is shown in Table III.

214 shell gaps which are larger than 1 MeV in the $^{348}138$ nucleus [see Figs. 10(a) and 10(b)]. A similar situation is also seen in the $^{466}156$ nucleus. In this nucleus, the bands of proton $(Z = 130, 132, 134, 136)$, $(Z = 142, 144, 146, 148)$, $(Z = 156, 158)$, and $(Z = 168, 170)$ shell gaps are formed because of the presence of the bunches of four single-particle states with relatively low Λ values located between them. The energies of these bunches slightly decrease with increasing absolute value of β_2 [see Fig. 11(a)]. Note that some of these gaps reach almost 2 MeV in size. Smaller neutron gaps with size of around 1 MeV and below are seen at $N = 294$, 296, 302, 314, and 318 and contrary to the proton subsystem they do not form the bands of shell gaps [see Fig. 11(b)].

The obtained results for the shell structure of toroidal nuclei allow us to understand its contribution into the stability of toroidal shapes with respect to breathing deformations. For example, LEMAS in the $^{348}138$ nucleus corresponds to the situation in which proton and neutron Fermi levels are located in the middle of the region of low density of single-particle states in the vicinity of the $Z = 134$ and $N = 210$ gaps, respectively [see Figs. 10(a) and 10(b)]. Any increase or decrease of the β_2 value from the one corresponding to LEMAS will lead to the increase of the density of the single-particle states in the vicinities of respective Fermi levels. This effect is especially pronounced for the neutron subsystem. As a consequence, the LEMAS corresponds to the largest or near largest (in absolute sense) negative proton and neutron shell correction energies, while the deviation (in terms of β_2) from total energy minimum will lead to the reduction of these energies. This contributes to the stability of toroidal shapes with respect to breathing deformations. However, as illustrated by the case of the $^{466}156$ nucleus, the contribution of shell correction effects to the stability of the nuclei is expected to depend on proton and neutron numbers. In this nucleus, the neutron Fermi level at LEMAS is located at high density of the neutron single-particle states [see Fig. 11(b)], which likely leads to positive neutron shell correction energies. In contrast, shell correction energies will be large and negative in the proton subsystem since the proton Fermi level is located in the vicinity of large $Z = 156$ gap [see Fig. 11(a)]. Note that this gap is so large that proton pairing collapses at the β_2 values near LEMAS; this is seen from the fact that the energy of the proton Fermi level coincides with the energy of the single-particle state located below the $Z = 156$ gap. When pairing collapses, the transition from Hartree-Bogoliubov formalism with pairing to the Hartree formalism without pairing takes place [29]. In the latter one, the Fermi level coincide with the position of the highest occupied level in the lowest in energy nucleonic configuration [18].

The same features are also active in respect of the stability of toroidal nuclei in sausage deformation degree of freedom. This is because of two factors. First, the shell gaps in the breathing degree of freedom are also the shell gaps in the sausage degree of freedom (see Sec. IV D in Ref. [5]). Second, as shown in toroidal harmonic oscillator shell model for particle numbers of interest, the increase of sausage deformations σ_λ of multipolarities $\lambda = 1$, 2, and 3 from zero to some finite values leads to washing out of these shell gaps and an increase

of the density of the single-particle states in the vicinity of the Fermi level (see Figs. 21, 22, and 23 in Ref. [5]). Let us consider the nuclei in which the proton and neutron Fermi levels of the LEMAS solution are located in the region of low density of the single-particle states. In these nuclei, the shell correction energy is negative at $\sigma_\lambda = 0$ but it will either be reduced in absolute value or become positive when sausage deformations become nonzero. Thus, the instability in the breathing degree of freedom which exists on the level of liquid drop is counterbalanced in these nuclei by the quantum shell effects. The balance of these two contributions defines whether the toroidal nucleus is stable with respect to sausage deformations or not. Fully quantum mechanical calculations based on DFT are needed to establish the stability of a given nucleus with respect of sausage deformations. However, the analysis of the shell structure and the level density of the single-particle states in the vicinity of the proton and neutron Fermi levels provides useful information on whether a given nucleus could potentially be stable with respect of sausage deformations. For example, as discussed above, such an analysis for the $^{348}138$ nucleus shows low densities of the single-particle states in the vicinity of proton and neutron Fermi levels and indeed the RMF+BCS calculations of Refs. [1,2] reveal the stability of toroidal shapes in this nucleus with respect to even-multipole sausage deformations.

Figures 10 and 11 reveal some global bunching of the pairs of almost degenerate in energy single-particle states of opposite parities. For example, such bunches of the states are seen in the proton subsystem of the $^{348}138$ nucleus at the energies ≈ -19, ≈ -14, ≈ 0, and ≈ 4 MeV for $\beta_2 = -5.0$ [see Figs. 10(c) and 10(e)]. The density of the single-particle states is high in these bunches and thus it is reasonable to expect that the shell correction energy E_{shell} will be positive when the Fermi level is located near or within these bunches. For such a situation, it is reasonable to expect that the quantum shell effects will not help stabilize toroidal shapes with respect to sausage deformations. With decreasing absolute value of β_2, the energies of these bunches of the single-particle states go down [see Figs. 10(c) and 10(e)]. However, these bunches and the low-density single-particle structure between them persist down to β_2 values, corresponding to the transition from toroidal to concave disk shapes. The density of the single-particle states is low between these bunches and it is reasonable to expect that for the majority of the combinations of particle number and β_2 the E_{shell} values will be negative when the Fermi level is located in this region. These features are the manifestation of so-called supershell structure, which has been discussed in the case of ellipsoidal-like shapes in Ref. [57].

There is a drastic difference in the behavior of neutron and proton Fermi levels as a function of the β_2 value (see Figs. 10 and 11). The neutron Fermi level is more or less constant as a function of β_2. As a consequence, the calculated two-neutron drip line for toroidal shapes is close to the extrapolation of this line for ellipsoidal-like shapes (see Fig. 2). In contrast, the proton Fermi level dives deeper into nucleonic potential with increasing absolute value of β_2; it is lower by approximately 5 MeV for toroidal shapes with large aspect ratio as compared with its position for biconcave disk shapes. As a consequence, the transition to toroidal shapes in hyperheavy nuclei creates a substantial expansion (the area between black solid and orange dashed lines in Fig. 2) of the nuclear landscape.

There are drastic changes in the single-particle structure of the $^{348}138$ nucleus at $\beta_2 \approx -1.15$ and $\beta_2 \approx -1.85$ [see Figs. 10(c), 10(d), 10(e), and 10(f)]. The first change is related to the transition from biconcave disk shape to toroidal one (which is equivalent to an opening of the hole in the center of biconcave disk shape). The second one is associated with the redistribution of the proton density in the torus caused by the change of the occupation of the single-particle orbitals. This density is asymmetric with respect to the axis of torus tube and has a maximum closer to an outer edge of the torus for the β_2 values ranging from ≈ -1.15 down to ≈ -1.85. However, it becomes almost symmetric with respect to the axis of the torus tube for $\beta_2 \leqslant -1.85$. Note that similar changes in the single-particle structure are seen at $\beta_2 \approx -1.1$, $\beta_2 \approx -1.8$, and $\beta_2 \approx -2.7$ in the $^{466}156$ nucleus [see Figs. 11(c), 11(d), 11(e), and 11(f)] and their origins are similar to the ones discussed above in the $^{348}138$ nucleus.

In order to find potentially most stable toroidal nuclei, two-proton $S_{2p}(Z,N)$ and two-neutron $S_{2n}(Z,N)$ separation energies

$$\begin{aligned} S_{2n}(Z,N) &= B(Z,N) - B(Z,N-2), \\ S_{2p}(Z,N) &= B(Z,N) - B(Z-2,N), \end{aligned} \tag{7}$$

and the $\delta_{2n}(Z,N)$ and $\delta_{2p}(Z,N)$ quantities defined as

$$\begin{aligned} \delta_{2n}(Z,N) &= S_{2n}(Z,N) - S_{2n}(Z,N-2), \\ \delta_{2p}(Z,N) &= S_{2p}(Z,N) - S_{2p}(Z-2,N), \end{aligned} \tag{8}$$

are plotted in Fig. 15 for the region with ($Z = 132$–144, $N = 204$–228). Here $B(Z,N)$ is the binding energy. The separation energies show a sudden drop at the shell gaps, if they are large. If the variations of the level density are less pronounced, the $\delta_{2n}(Z,N)$ and $\delta_{2p}(Z,N)$ quantities related to the derivatives of the separation energies are more sensitive indicators of the localizations of the shell gaps (see discussion in the Appendix of Ref. [58]). They also provide the information on average density of the single-particle states.

The presence of the neutron gap at $N = 210$ for toroidal shapes is visible in Figs. 15(a) and 16(a) in the $Z = 126$–136 nuclei. The $\delta_{2n}(Z,N)$ values for neutron numbers away from $N = 210$ are low, which is indicative of high density of neutron single-particle states below and above the $N = 210$ shell gap. These features correlate with the ones seen in the Nilsson diagram [see Fig. 10(b)].

In contrast, the $S_{2p}(Z,N)$ and $\delta_{2p}(Z,N)$ values [see Figs. 15(b) and 16(b)] are relatively smooth functions of proton number which indicates that the average density of proton single-particle states remains more or less constant. However, on average the $\delta_{2p}(Z,N)$ values are substantially higher than the $\delta_{2n}(Z,N)$ ones; only in the region of the peak of $\delta_{2n}(Z,N)$ at $N = 210$ they are comparable (see Fig. 16). This clearly indicates that the density of proton single-particle states is low in a wide range of proton numbers and this observation is supported by the comparison of Figs. 10(a) and 10(b). Note that the peak of $\delta_{2p}(Z,N) \approx 1.3$ MeV is seen for neutron numbers

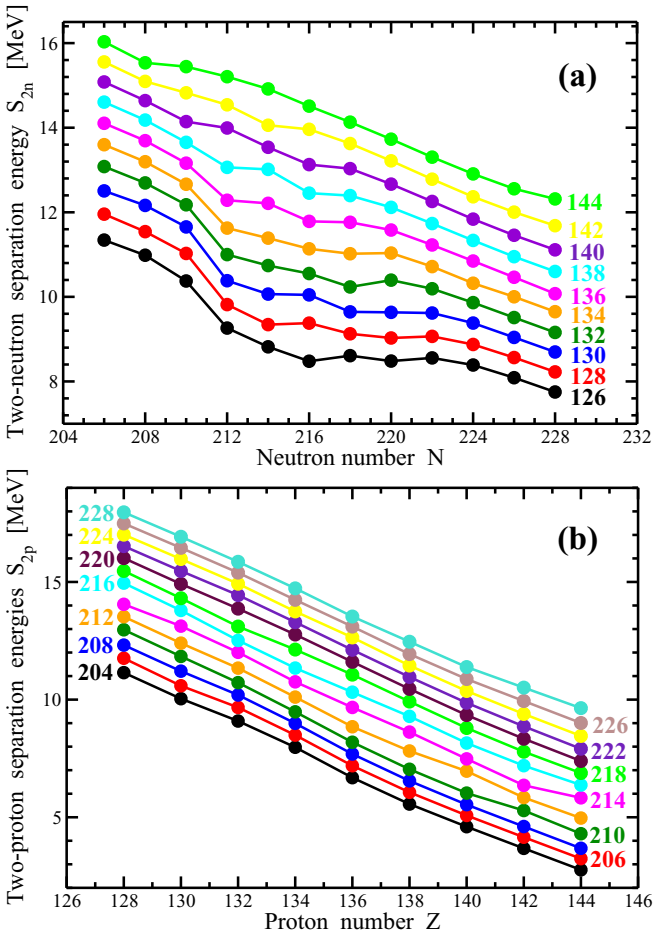

FIG. 15. Two-neutron $[S_{2n}(Z,N)]$ and two-proton $[S_{2p}(Z,N)]$ separation energies given for different isotopic (isotonic) chains as a function of the neutron (proton) number. The lines are labeled by respective proton (a) and neutron (b) numbers.

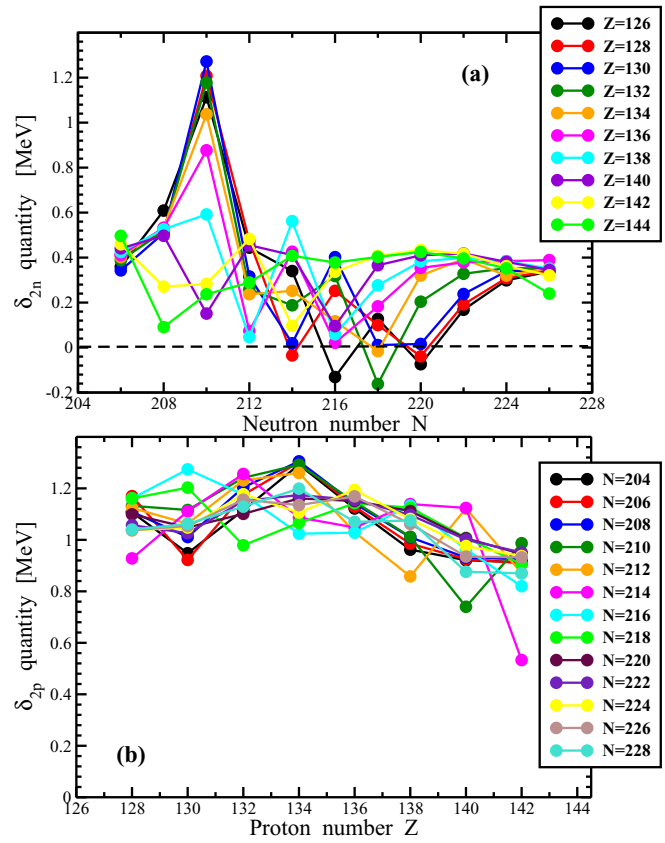

FIG. 16. The $\delta_{2n}(Z,N)$ and $\delta_{2p}(Z,N)$ quantities for the toroidal nuclei in the ($Z = 126$–144, $N = 204$–228) region.

$N = 204$–212 [see Fig. 16(b)], suggesting extra stability of these nuclei.

The combination of proton and neutron shell effects should lead to enhanced stability of specific nuclei. As a result, features discussed above are most likely reasons why the fission barrier is higher in the $N = 210$ ^{348}138 nucleus as compared with the $N = 220$ ^{354}134 one.

C. Functional dependence of the results

When considering the predictions for toroidal hyperheavy nuclei and their shell structure, it is important to evaluate their dependence on the employed functional. So far, all predictions for such nuclei presented in Refs. [1,2] and in the present paper were obtained with the CEDF DD-PC1. To study functional dependence of the predictions, we perform additional calculations for the ^{348}138 and ^{466}156 nuclei with the NL3* [32], PC-PK1 [37], DD-ME2 [35], and DD-MEδ [36] functionals and compare their results with the ones obtained with DD-PC1 earlier. These five state-of-the-art functionals represent three major classes of CDFT models [21] and have been globally tested in Refs. [21,23,25,59,60]. Note that in this set of the functionals the CEDF DD-PC1 and PC-PK1 provide better descriptions of binding energies on a global scale as compared with other functionals.

The deformation energy curves obtained with these functionals are presented in Fig. 17. In both nuclei and in terms of relative energies of the minima corresponding to toroidal and ellipsoidal-like shapes, there is a large similarity of the results obtained with point-coupling models DD-PC1 and PC-PK1 as well as with nonlinear meson-nucleon coupling model NL3* on the one hand and those obtained with density-dependent meson-exchange models DD-ME2 and DD-MEδ on the other hand. In the latter type of the models, the toroidal shapes are less energetically favored with respect to ellipsoidal-like shapes as compared with former models. For example, in the ^{348}138 nucleus, the fat toroidal shapes corresponding to the minimum *A* are more (less) energetically favored as compared with biconcave disk shapes corresponding to minimum *B* in the calculations with DD-PC1 and PC-PK1 (DD-ME2 and DD-MEδ) functionals. Note that these two minima are located at approximately the same energies in the calculations with the NL3* functional [see Fig. 17(a)]. However, this difference in the predictions of relative energies of the minima *A* and *B* is not principal because the minimum *B* is not stable with respect of triaxial distortions in the calculations with DD-PC1 functional (see Ref. [1]) and the same situation is expected for other functionals because of the similarity of underlying shell structure. On the other hand, the minimum *A* is relatively

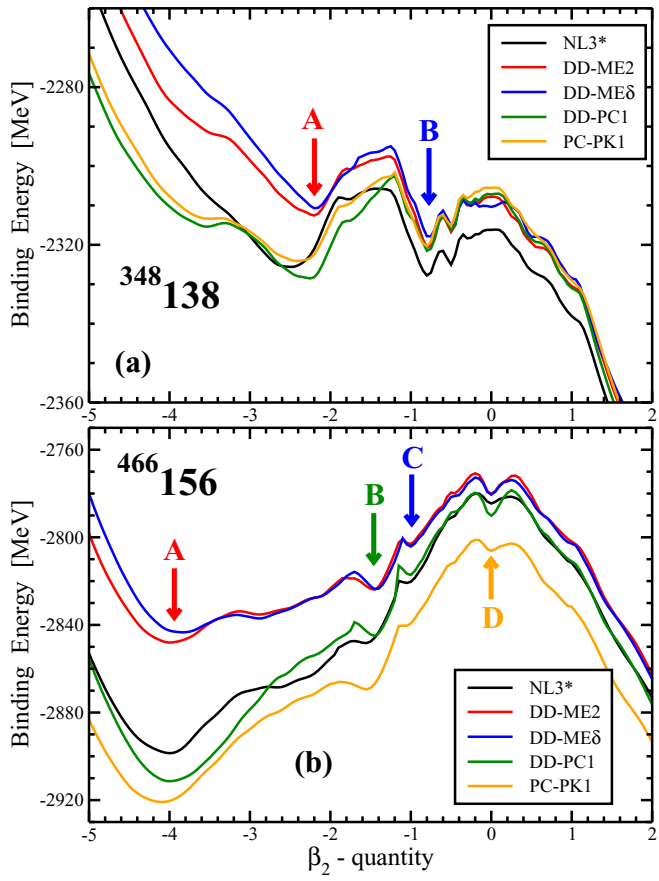

FIG. 17. The deformation energy curves obtained in axial RHB calculations with indicated CEDFs. The local and global minima are indicated by the arrows with letters. The same labeling of minima as shown in Fig. 1 is used for the ^{466}156 nucleus.

stable with respect of even-multipole sausage deformations in the calculations with DD-PC1 (see Refs. [1,2]), and because of the similarity of the underlying toroidal shell structure (see discussion of Fig. 18 below) it is reasonable to expect that this is also the case for the remaining functionals.

A situation similar to the ^{348}138 nucleus holds also in the ^{466}156 one. This is because toroidal shapes are more energetically favored as compared with ellipsoidal-like ones in the calculations with CEDFs DD-PC1, PC-PK1, and NL3* than in those employing DD-ME2 and DD-MEδ functionals [see Fig. 17(b)]. For example, the energy difference ΔE_{diff} between the minimum A corresponding to thin toroidal shapes and the minimum D corresponding to spherical shapes is approximately 117 MeV in the calculations with the first group of the functionals and only approximately 67 MeV in the calculations with the second group. Note that these differences cannot be explained by the differences in nuclear matter properties of the functionals since they are similar (quite different) in the pair of the DD-PC1 and DD-ME2 (DD-PC1 and PC-PK1) functionals (see Ref. [25]) which provide the ΔE_{diff} values, which differ by 53.4 MeV (by only 6.5 MeV).

These differences between the functionals, related to the relative energies of the minima corresponding to toroidal and ellipsoidal-like shapes, are expected to affect the position of the boundary between ellipsoidal-like and toroidal shapes in the nuclear landscape (see Fig. 2 in the present paper and the discussion in Sec. XII of Ref. [2]). However, this boundary depends not only on relative energies of these two types of the shapes but also on the stability of ellipsoidal-like shapes with respect of fission (see Ref. [2]). There is a quite substantial dependence of the fission barrier heights for ellipsoidal-like shapes on CEDF with the PC-PK1 and NL3* (DD-ME2 and DD-PC1) functionals providing the lowest (highest) barrier heights for superheavy nuclei among the CEDFs considered in Ref. [3] and a similar situation is also expected in the hyperheavy nuclei.

Despite the above-mentioned differences, there are large similarities between the results of the calculations obtained with five functionals. For the first time, the results presented in Fig. 17 confirm that the transition from ellipsoidal-like to toroidal shapes with increasing proton number Z does not depend on CEDF. The presence of similar local minima in deformation energy curves (such as the minima A, B, C, and D in the ^{466}156 nucleus and the minima A and B in the ^{348}138 nucleus) with similar equilibrium β_2 values presented in Fig. 17 clearly suggest the similarity of underlying shell structure in all employed functionals. Note that in a few cases such minima are shoulder-like in deformation energy curves without a sufficient barrier on one side: These are the minimum C in the calculations with NL3* and PC-PK1 and the minimum B in the calculations with NL3* [(see Fig. 17(b)].

The analysis of toroidal shell structure of the ^{348}138 and ^{466}156 nuclei obtained with the NL3*, PC-PK1, DD-ME2, and DD-MEδ functionals reveals the same general features as those discussed in Sec. IV B for the DD-PC1 functional. Thus, we will focus on fine details of the shell structure of these nuclei in the vicinity of the respective Fermi levels at the LEMAS of the minimum A in these two nuclei (see Fig. 17) since they are responsible for potential stability of respective toroidal shapes. The Nilsson diagrams for these four CEDFs are shown in Figs. 18 and 19; they can be compared with those obtained for DD-PC1 and presented in Figs. 10(a), 10(b), 11(a), and 11(b). This comparison reveals significant similarities between the results of the calculations obtained with different functionals.

For example, in the ^{348}138 nucleus, the proton Fermi level E_F at LEMAS is located in the region of reduced density of proton single-particle states between shell gaps at $Z = 134$ and $Z = 140$ [see Fig. 10(a)] in the calculations with the DD-PC1 functionals. A similar situation exists also in the calculations with NL3*, PC-PK1, DD-ME2, and DD-MEδ CEDFs [see Figs. 18(a), 18(c), 18(e), and 18(g)]. In this nucleus, the neutron Fermi level is located in the middle of substantial $N = 210$ toroidal shell gap in the calculations with DD-PC1 [see Fig. 10(a)] and DD-ME2 and DD-MEδ [see Figs. 18(e) and 18(g)], but it is shifted to the region of somewhat higher density of the neutron single-particle states below the $N = 214$ toroidal shell gap in the calculations with NL3* and PC-PK1 [see Figs. 18(b) and 18(d)]. These results suggest that two-proton separation energies $S_{2p}(Z, N)$ and the $\delta_{2p}(Z, N)$ quantities (see the discussion in the end of Sec. IV B) should be very similar for all five

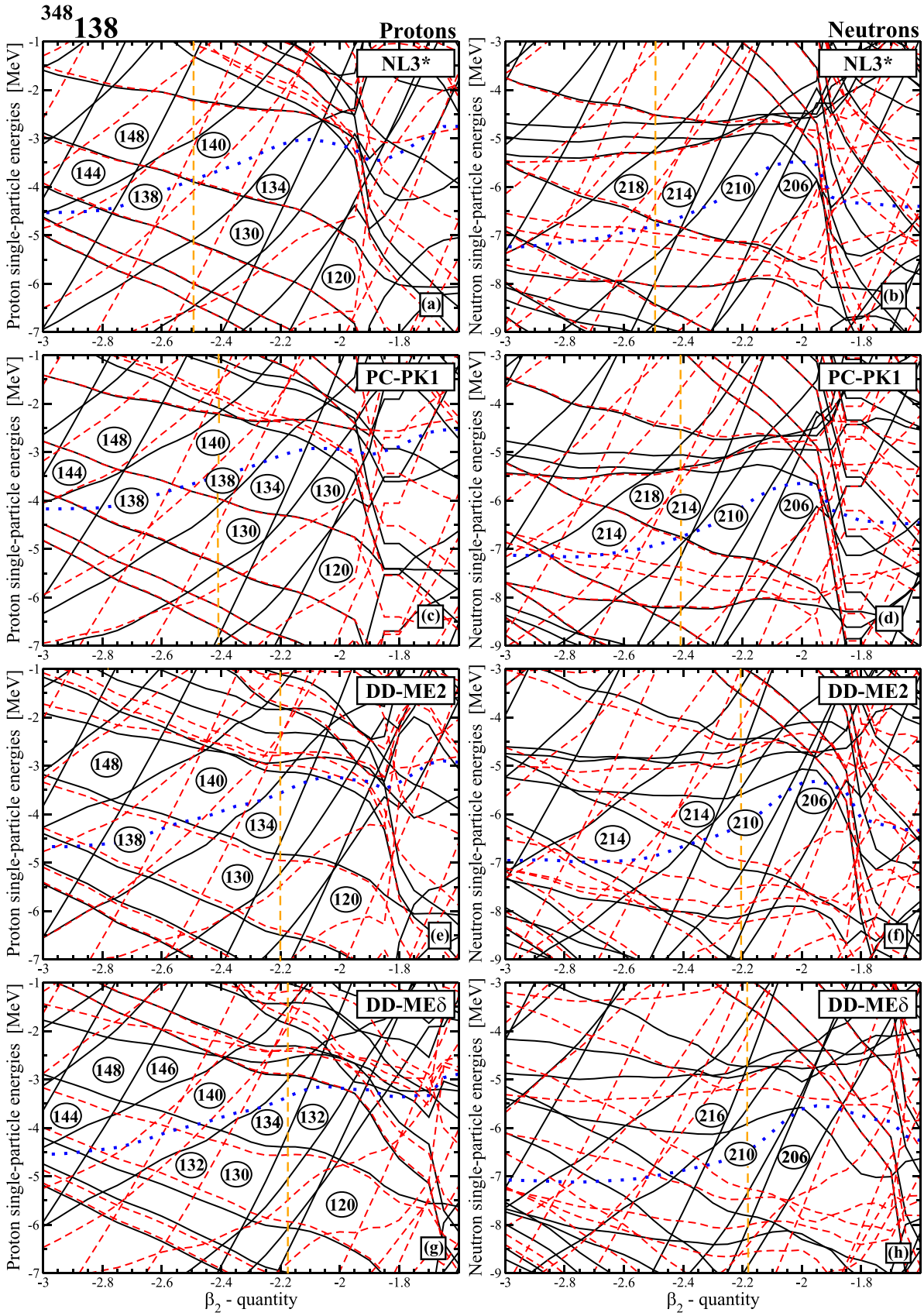

FIG. 18. The same as Figs. 10(a) and 10(b) but for the results obtained with indicated CEDFs. The vertical dashed orange lines are drawn at the β_2 values corresponding to LEMAS.

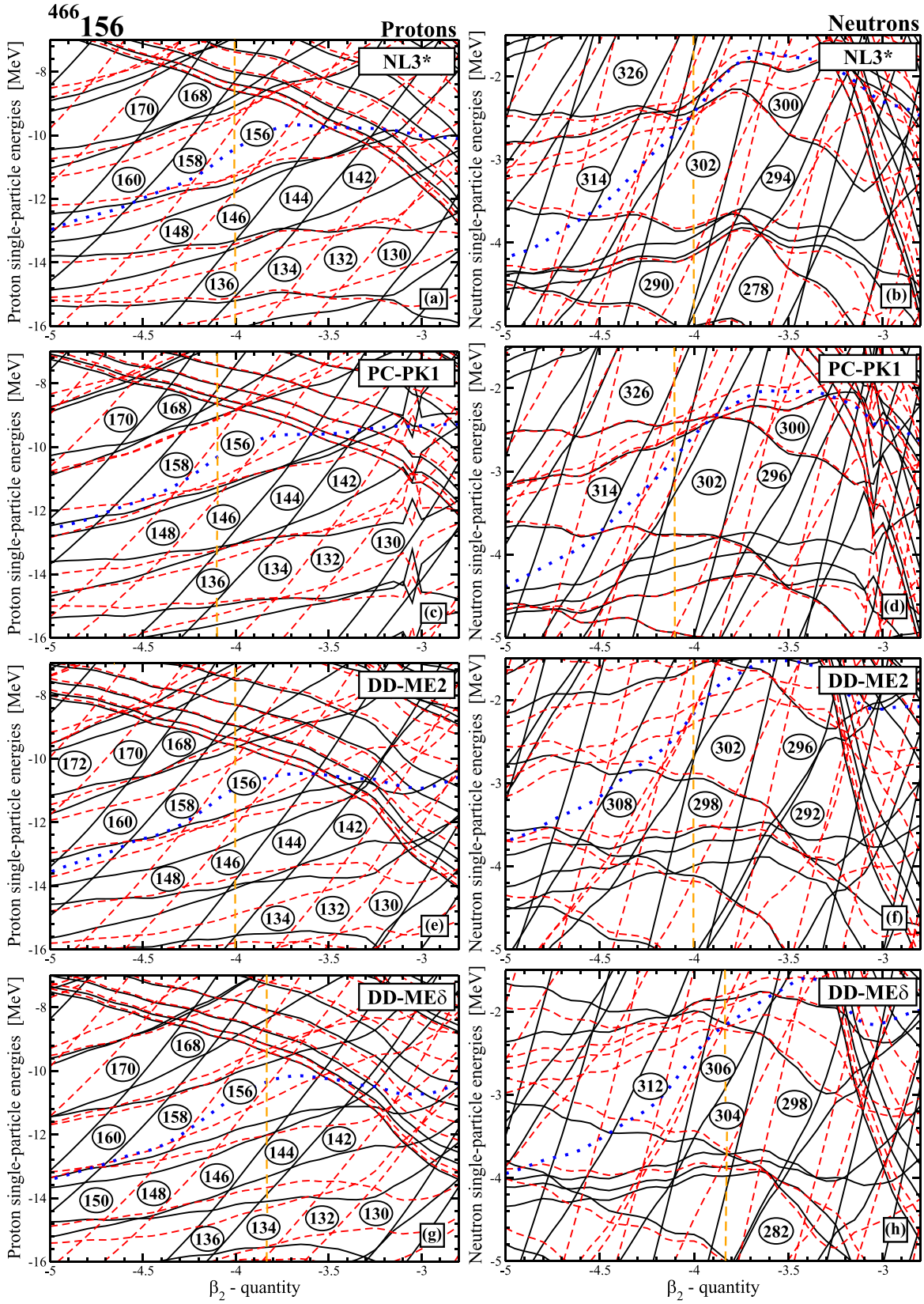

FIG. 19. The same as Figs. 11(a) and 11(b) but for the results obtained with indicated CEDFs. The vertical dashed orange lines are drawn at the β_2 values corresponding to LEMAS.

employed functionals. The same is true for related neutron $S_{2n}(Z,N)$ and $\delta_{2n}(Z,N)$ values obtained in the calculations with DD-PC1, DD-ME2, and DD-MEδ, which are expected to reveal the presence of the $N=210$ toroidal shell gap [see Fig. 16(b)]. However, it is quite likely that the peak in the $\delta_{2n}(Z,N)$ values visible at $N=210$ in the calculations with DD-PC1 [see Fig. 16(a)] will be moved to $N\approx 214$ and substantially washed out in the calculations with NL3* and PC-PK1.

A similar situation exists also in the $^{466}156$ nucleus. The bands of proton ($Z=130$, 132, 134, 136), ($Z=142$, 144, 146, 148), ($Z=156$, 158, 160), and ($Z=168$, 170) shell gaps, formed because of the presence of the bunches of single-particle states with relatively low Λ values located between them, exist in all five functionals [see Figs. 11(a), 19(a), 19(c), 19(e), and 19(g)]. Note that some of these gaps reach almost 2 MeV in size. The proton Fermi level at LEMAS is located either in the middle of large $Z=156$ shell gap in the NL3*, PC-PK1, DD-ME2, and DD-MEδ functionals or at the bottom of this shell gap in the DD-PC1 CEDF and thus shell correction energies will be large and negative in the proton subsystem in all functionals.

Smaller neutron shell gaps with the size of around 1 MeV and below are seen at $N=294$, 296, 302, 314, 318 in DD-PC1 [Fig. 11(a)], at $N=278$, 290, 294, 300, 302, 314, 318 in NL3* [Fig. 19(b)], at $N=296$, 300, 302, 314, 326 in PC-PK1 [Fig. 19(d)], at $N=292$, 296, 298, 302, 308 in DD-ME2 [Fig. 19(f)], and at $N=282$, 298, 304, 306, 312 in DD-MEδ [Fig. 19(h)], and contrary to the proton subsystem they do not form the bands of shell gaps. Considering the relatively small size of neutron shell gaps, larger (as compared with the proton subsystem) dependence of the predictions for neutron shell gaps on the functional is expected. These differences are not critical since in all functionals the neutron Fermi level at LEMAS is located at high density of the neutron single-particle states, which likely leads to positive neutron shell correction energies.

The results presented in Fig. 17 clearly indicate the stability of the nuclei under discussion with respect to breathing deformation in all employed functionals. The similarity of the shell structure in all five functionals strongly suggests that the considerations provided in Sec. IV B on potential stability with respect to sausage deformations of the nuclei under study in the case of CEDF DD-PC1 are also applicable for the NL3*, PC-PK1, DD-ME2, and DD-MEδ functionals.

V. CONCLUSIONS

In conclusion, the detailed investigation of the properties of spherical and toroidal hyperheavy even-even nuclei and their underlying shell structure have been performed in the framework of covariant density functional theory. The following conclusions have been obtained:

(1) Proton $Z=154$, 186 and neutron $N=228$, 308, and 406 spherical shell gaps exist in all employed CEDFs. Their combinations define the islands of stability of spherical hyperheavy nuclei. The sizes of these gaps (both actual $\Delta E_{\rm gap}$ and scaled $\Delta E_{\rm gap}A^{1/3}$) are larger than those of $Z=120$ and $N=184$ in superheavy nuclei. This suggests that some spherical hyperheavy nuclei may be more stable than superheavy ones. Systematic theoretical uncertainties in the predictions of the sizes of spherical shell gaps in hyperheavy nuclei are smaller than those in superheavy nuclei and experimentally known nuclei.

(2) Detailed calculations in extremely large basis have allowed us to establish for the first time the general trends of the evolution of toroidal shapes in the $Z\approx$ 130–180 region of the nuclear chart. Although they have been performed only for selected $Z=136$, 146, 156, 166, and 176 nuclei with the step in neutron number of $\Delta N=10$, their distribution in the nuclear chart between two-proton and two-neutron drip lines and deformation energy curves of these nuclei is such that they allow us to safely extrapolate major conclusions for all nuclei in the above-mentioned region. The most compact fat toroidal nuclei are located in the $Z\approx 136, N\approx 206$ region (see Fig. 8). Thin toroidal nuclei with large R/d aspect ratio become dominant with increasing proton number and on moving toward proton and neutron drip lines.

(3) All the nuclei in the $Z\approx$ 130–180 region located between neutron and proton drip lines are expected to be stable with respect to breathing deformations. Because of numerical difficulties, it is much more problematic to answer the question on their stability with respect to sausage deformations. However, the analysis of theoretical and experimental studies of toroidal liquid droplets as well as the results on the stability of the $^{354}134$ and $^{348}138$ nuclei with respect to even-multipole sausage deformations obtained in Refs. [1,2] suggest that fat toroidal nuclei located in the $Z\approx 136, N\approx 210$ region are potentially more stable with respect to sausage deformations than thin toroidal nuclei located outside of this region. Nevertheless, future fully quantum mechanical calculations based on DFT are needed to establish the stability of specific toroidal nuclei since the quantum shell effects can counterbalance the instabilities with respect of sausage deformations [5].

(4) Toroidal shell structure (especially the one for the shapes with large R/d aspect ratio) has much more pronounced regular features as compared with the shell structure of deformed ellipsoidal-like nuclei. Global bunching of the pairs of almost degenerate single-particle states of opposite parities leads to an appearance of supershell structure. These features are mostly driven by the existence of the two classes of the pairs of the orbitals at toroidal shapes. The pairs of the orbitals with dominant structure of $\Omega[N,n_z,\Lambda]$ and $(\Omega+1)[N,n_z,\Lambda]$ with $n_z=0$ belong to the first class. The second class is formed by almost degenerate in energy single-particle states of opposite parities with dominant structures of the wave functions given by $\Omega[N,n_z,\Lambda]$ and $\Omega[N',n'_z,\Lambda']$ for which the conditions $N'=N\pm 1$, $|\Lambda'-\Lambda|=0$ or 1, and $|n'_z-n_z|=0$ or 1 are typically satisfied.

(5) As illustrated by discussed cases, at LEMAS large shell gaps and/or low density of the single-particle states appear at least in one of the subsystems (proton and/or neutron) in the vicinity of its Fermi level. These shell gaps are also the gaps in breathing and sausage degrees of freedom [5]. If the Fermi level in a given subsystem is located in the vicinity of the large shell gap or low density of the single-particle states, quantum shell effects will act against the instabilities in breathing and sausage deformations. These stabilizing effects will be definitely enhanced if both proton and neutron subsystems are characterized by such features.

(6) However, the analysis of the Nilsson diagrams for all nuclei calculated in Fig. 8 shows that in many of these nuclei the level densities are high near the proton and neutron Fermi levels at LEMAS. In reality, such a situation becomes much more frequent with increasing proton and neutron numbers and respective rise of the single-particle level densities. The reason is quite simple: The β_2 value of LEMAS is defined mostly by the competition of nuclear surface tension and Coulomb interaction and the shell correction effects play only a secondary role here. As a result, such nuclei are expected to be unstable with respect to sausage deformations. Thus, it is reasonable to expect the existence of the "continent" of stability of toroidal nuclei in low-Z systems which is replaced by the "isolated islands" of their stability in higher Z nuclei located in the "sea of the instability."

The problem of the stability of toroidal nuclei with respect of sausage deformations emerges as a major obstacle in their study. There are several possible ways to investigate such instabilities. One is based on the analysis of time evolution of the toroidal nucleus after some external disturbance of equilibrium shape in time-dependent Hartree-(Fock)-Bogoliubov framework formulated in coordinate representation. However, the sizes of thin toroidal nuclei are significantly larger than those of ellipsoidal ones and the tube of the torus of such nuclei is characterized by a small radius and rapid change of the densities. These factors would require a very large three-dimensional box with small steps in each direction. At present, it is not clear whether such calculations are numerically feasible.

An alternative possibility is to rewrite existing RHB computer codes on the basis of toroidal harmonic oscillator potential and to study "fission" barriers in respective sausage deformations. Since this is a native basis for toroidal shapes, it is reasonable to expect that sufficient numerical accuracy could be achieved at significantly lower size of the toroidal harmonic oscillator basis as compared with existing computers codes formulated in the traditional harmonic oscillator basis, which is more suitable for ellipsoidal-like shapes. For example, in the latter codes the $N_F = 20$ fermionic shells are sufficient for the description of spherical and ellipsoidal shapes in the $^{466}156$ nucleus but $N_F = 30$ is required for the description of toroidal shapes [2]. The use of a toroidal harmonic oscillator basis would reverse the situation and we hope the basis with $N_F = 20$ will be sufficient for the description of toroidal shapes near LEMAS and their instabilities with respect to sausage deformations. Our experience tells us that numerical calculations in such a basis are feasible with existing high-performance computers.

The instabilities of toroidal nuclei with respect to sausage deformations can potentially be studied by means of three-dimensitional lattice (3D lattice) method suggested in Ref. [61]. For example, this method has been used for the investigation of the stability of linear chain structure of three α clusters in ^{12}C against bending and fission in the framework of cranking CDFT in Ref. [62].

ACKNOWLEDGMENTS

This material is based upon work supported by the U.S. Department of Energy, Office of Science, Office of Nuclear Physics under Award No. DE-SC0013037.

[1] A. V. Afanasjev, S. E. Agbemava, and A. Gyawali, Hyperheavy nuclei: Existence and stability, Phys. Lett. B **782**, 533 (2018).
[2] S. E. Agbemava, A. V. Afanasjev, A. Taninah, and A. Gyawali, Extension of the nuclear landscape to hyperheavy nuclei, Phys. Rev. C **99**, 034316 (2019).
[3] A. V. Afanasjev, S. E. Agbemava, and A. Taninah, Exploring nuclear exotica at the limits, Acta Phys. Pol. B Proc. Suppl. **13**, 347 (2020).
[4] H. Abusara, A. V. Afanasjev, and P. Ring, Fission barriers in covariant density functional theory: Extrapolation to superheavy nuclei, Phys. Rev. C **85**, 024314 (2012).
[5] C. Y. Wong, Toroidal and spherical bubble nuclei, Ann. Phys. **77**, 279 (1973).
[6] M. Jehser and C. N. Likos, Aggregation shapes of amphiphilic ring polymers: From spherical to toroidal micelles, Colloid Polym. Sci. **298**, 735 (2020).
[7] D. Wang, C. Liu, H. Liu, J. Han, and S. Zhang, Wave dynamics on toroidal surface, Opt. Express **26**, 17820 (2018).
[8] M. Zabarankin, Liquid toroidal drop under uniform electric field, Proc. R. Soc. A **473**, 20160633 (2017).
[9] A. Daskalaki, *Handbook of Research on Systems Biology Applications in Medicine* (Hershey, London, 2009).
[10] A. Leforestier and F. Livolant, Structure of toroidal DNA collapsed inside the phage capsid, Proc. Nat. Acad. Sci. USA **106**, 9157 (2009).
[11] M. Warda, Toroidal structure of super-heavy nuclei in the HFB theory, Int. J. Mod. Phys. E **16**, 452 (2007).
[12] A. Staszczak and C. Y. Wong, Toroidal super-heavy nuclei in Skyrme Hartree-Fock approach, Acta Phys. Pol. **40**, 753 (2009).
[13] A. Staszczak and C.-Y. Wong, A region of high-spin toroidal isomers, Phys. Lett. B **738**, 401 (2014).
[14] T. Ichikawa, K. Matsuyanagi, J. A. Maruhn, and N. Itagaki, High-spin torus isomers and their precession motions, Phys. Rev. C **90**, 034314 (2014).
[15] A. Kosior, A. Staszczak, and C.-Y. Wong, Toroidal nuclear matter distributions of superheavy nuclei from constrained

Skyrme-HFB calculations, Acta Phys. Pol. B Proc. Suppl. **10**, 249 (2017).
[16] W. Nazarewicz, M. Bender, S. Cwiok, P. H. Heenen, A. T. Kruppa, P.-G. Reinhard, and T. Vertse, Theoretical description of superheavy elements, Nucl. Phys. A **701**, 165c (2002).
[17] A. Staszczak, C.-Y. Wong, and A. Kosior, Toroidal high-spin isomers in the nucleus $^{304}120$, Phys. Rev. C **95**, 054315 (2017).
[18] A. V. Afanasjev, D. B. Fossan, G. J. Lane, and I. Ragnarsson, Termination of rotational bands: Disappearance of quantum many-body collectivity, Phys. Rep. **322**, 1 (1999).
[19] X. G. Cao, E. J. Kim, K. Schmidt, K. Hagel, M. Barbui, J. Gauthier, S. Wuenschel, G. Giuliani, M. R. D. Rodriguez, S. Kowalski, H. Zheng, M. Huang, A. Bonasera, R. Wada, N. Blando, G. Q. Zhang, C. Y. Wong, A. Staszczak, Z. X. Ren, Y. K. Wang, S. Q. Zhang, J. Meng, and J. B. Natowitz, Examination of evidence for resonances at high excitation energy in the 7α disassembly of ^{28}Si, Phys. Rev. C **99**, 014606 (2019).
[20] A. A. Fragkopoulos, E. Pairam, E. Berger, P. N. Segre, and A. Fernandez-Nieves, Shrinking instability of toroidal droplets, Proc. Nat. Acad. Sci. USA **114**, 2871 (2017).
[21] S. E. Agbemava, A. V. Afanasjev, D. Ray, and P. Ring, Global performance of covariant energy density functionals: Ground state observables of even-even nuclei and the estimate of theoretical uncertainties, Phys. Rev. C **89**, 054320 (2014).
[22] T. Nikšić, D. Vretenar, and P. Ring, Relativistic nuclear energy density functionals: Adjusting parameters to binding energies, Phys. Rev. C **78**, 034318 (2008).
[23] S. E. Agbemava, A. V. Afanasjev, T. Nakatsukasa, and P. Ring, Covariant density functional theory: Reexamining the structure of superheavy nuclei, Phys. Rev. C **92**, 054310 (2015).
[24] S. E. Agbemava, A. V. Afanasjev, D. Ray, and P. Ring, Assessing theoretical uncertainties in fission barriers of superheavy nuclei, Phys. Rev. C **95**, 054324 (2017).
[25] A. V. Afanasjev and S. E. Agbemava, Covariant energy density functionals: Nuclear matter constraints and global ground state properties, Phys. Rev. C **93**, 054310 (2016).
[26] V. Prassa, T. Nikšić, G. A. Lalazissis, and D. Vretenar, Relativistic energy density functional description of shape transitions in superheavy nuclei, Phys. Rev. C **86**, 024317 (2012).
[27] B.-N. Lu, E.-G. Zhao, and S.-G. Zhou, Potential energy surfaces of actinide nuclei from a multidimensional constrained covariant density functional theory: Barrier heights and saddle point shapes, Phys. Rev. C **85**, 011301 (2012).
[28] S. E. Agbemava, A. V. Afanasjev, and P. Ring, Octupole deformation in the ground states of even-even nuclei: A global analysis within the covariant density functional theory, Phys. Rev. C **93**, 044304 (2016).
[29] P. Ring and P. Schuck, *The Nuclear Many-Body Problem* (Springer-Verlag, Berlin, 1980).
[30] P. Bonche, H. Flocard, and P. H. Heenen, Solution of the Skyrme HF+BCS equation on a 3D mesh, Comput. Phys. Commun. **171**, 49 (2005).
[31] P.-G. Reinhard, M. Rufa, J. Maruhn, W. Greiner, and J. Friedrich, Nuclear ground state properties in a relativistic meson field model, Z. Phys. A **323**, 13 (1986).
[32] G. A. Lalazissis, J. König, and P. Ring, New parametrization for the Lagrangian density of relativistic mean field theory, Phys. Rev. C **55**, 540 (1997).
[33] G. A. Lalazissis, S. Karatzikos, R. Fossion, D. P. Arteaga, A. V. Afanasjev, and P. Ring, The effective force NL3 revisited, Phys. Lett. B **671**, 36 (2009).
[34] B. G. Todd-Rutel and J. Piekarewicz, Neutron-Rich Nuclei and Neutron Stars: A New Accurately Calibrated Interaction for the Study of Neutron-Rich Matter, Phys. Rev. Lett. **95**, 122501 (2005).
[35] G. A. Lalazissis, T. Nikšić, D. Vretenar, and P. Ring, New relativistic mean-field interaction with density-dependent meson-nucleon couplings, Phys. Rev. C **71**, 024312 (2005).
[36] X. Roca-Maza, X. Viñas, M. Centelles, P. Ring, and P. Schuck, Relativistic mean-field interaction with density-dependent meson-nucleon vertices based on microscopical calculations, Phys. Rev. C **84**, 054309 (2011).
[37] P. W. Zhao, Z. P. Li, J. M. Yao, and J. Meng, New parametrization for the nuclear covariant energy density functional with a point-coupling interaction, Phys. Rev. C **82**, 054319 (2010).
[38] T. Bürvenich, D. G. Madland, J. A. Maruhn, and P.-G. Reinhard, Nuclear ground state observables and QCD scaling in a refined relativistic point coupling model, Phys. Rev. C **65**, 044308 (2002).
[39] Y. Sugahara and H. Toki, Relativistic mean-field theory for unstable nuclei with non-linear sigma and omega terms, Nucl. Phys. A **579**, 557 (1994).
[40] S. Karatzikos, A. V. Afanasjev, G. A. Lalazissis, and P. Ring, The fission barriers in actinides and superheavy nuclei in covariant density functional theory, Phys. Lett. B **689**, 72 (2010).
[41] Y. Tian, Z. Y. Ma, and P. Ring, A finite range pairing force for density functional theory in superfluid nuclei, Phys. Lett. B **676**, 44 (2009).
[42] A. V. Afanasjev and O. Abdurazakov, Pairing and rotational properties of actinides and superheavy nuclei in covariant density functional theory, Phys. Rev. C **88**, 014320 (2013).
[43] J. Dobaczewski, A. V. Afanasjev, M. Bender, L. M. Robledo, and Y. Shi, Properties of nuclei in the nobelium region studied within the covariant, Skyrme, and Gogny energy density functionals, Nucl. Phys. A **944**, 388 (2015).
[44] B.-N. Lu, J. Zhao, E.-G. Zhao, and S.-G. Zhou, Multidimensionally constrained relativistic mean-field models and potential-energy surfaces of actinide nuclei, Phys. Rev. C **89**, 014323 (2014).
[45] A. V. Afanasjev and S. Frauendorf, Description of rotating $n = z$ nuclei in terms of isovector pairing, Phys. Rev. C **71**, 064318 (2005).
[46] Z. Yao and M. Bowick, The shrinking instability of toroidal liquid droplets in the Stokes flow regime, Eur. Phys. J. E **34**, 1 (2011).
[47] B. Darbois Texier, K. Piroird, D. Quéré, and C. Clanet, Inertial collapse of liquid rings, J. Fluid Mech. **717**, R3 (2013).
[48] H. Mehrabian and J. J. Feng, Capillary breakup of a liquid torus, J. Fluid Mech. **717**, 281 (2013).
[49] E. Pairam and A. Fernández-Nieves, Generation and Stability of Toroidal Droplets in a Viscous Liquid, Phys. Rev. Lett. **102**, 234501 (2009).
[50] J. D. McGraw, J. Li, D. L. Tran, A.-C. Shi, and K. Dalnoki-Veress, Plateau-Rayleigh instability in a torus: Formation and breakup of a polymer ring, Soft Matter **6**, 1258 (2010).
[51] A. Staszczak and C.-Y. Wong, Toroidal high-spin isomers in light nuclei with $n \neq z$, Phys. Scr. **90**, 114006 (2015).
[52] C.-Y. Wong and A. Staszczak, Shells in a toroidal nucleus in the intermediate-mass region, Phys. Rev. C **98**, 034316 (2018).
[53] W. Zhang, H.-Z. Liang, S.-Q. Zhang, and J. Meng, Search for ring-like nuclei under extreme conditions, Chin. Phys. Lett. **27**, 102103 (2010).

[54] A. Sobiczewski and K. Pomorski, Description of structure and properties of superheavy nuclei, Prog. Part. Nucl. Phys. **58**, 292 (2007).

[55] S. A. Giuliani, Z. Matheson, W. Nazarewicz, E. Olsen, P.-G. Reinhard, J. Sadhukhan, B. Schuetrumpf, N. Schunck, and P. Schwerdtfeger, Colloquium: Superheavy elements: Oganesson and beyond, Rev. Mod. Phys. **91**, 011001 (2019).

[56] R. A. Gherghescu, Deformed two-center shell model, Phys. Rev. C **67**, 014309 (2003).

[57] I. Ragnarsson, S. G. Nilsson, and R. K. Sheline, Shell structure in nuclei, Phys. Rep. **45**, 1 (1978).

[58] A. V. Afanasjev, T. L. Khoo, S. Frauendorf, G. A. Lalazissis, and I. Ahmad, Cranked relativistic Hartree-Bogoliubov theory: Probing the gateway to superheavy nuclei, Phys. Rev. C **67**, 024309 (2003).

[59] K. Q. Lu, Z. X. Li, Z. P. Li, J. M. Yao, and J. Meng, Global study of beyond-mean-field correlation energies in covariant energy density functional theory using a collective Hamiltonian method, Phys. Rev. C **91**, 027304 (2015).

[60] A. Taninah, S. E. Agbemava, and A. V. Afanasjev, Covariant density functional theory input for *r*-process simulations in actinides and superheavy nuclei: The ground state and fission properties, Phys. Rev. C **102**, 054330 (2020).

[61] Z. X. Ren, S. Q. Zhang, and J. Meng, Solving Dirac equations on a 3D lattice with inverse Hamiltonian and spectral methods, Phys. Rev. C **95**, 024313 (2017).

[62] Z. X. Ren, S. Q. Zhang, P. W. Zhao, N. Itagaki, J. A. Maruhn, and J. Meng, Stability of the linear chain structure for ^{12}C in covariant density functional theory on a 3D lattice, Sci. China: Phys., Mech. Astron. **62**, 112062 (2019).